# 13

# *Quantitative Polarimetry for Tissue Characterization and Diagnosis*

**David Layden**

*Department of Physics and Astronomy, University of Waterloo, 200 University Avenue West, Waterloo, Ontario N2L 3G1, Canada*

**Nirmalya Ghosh**

*Department of Physical Sciences, Indian Institute of Science Education and Research (IISER), Kolkata, Mohanpur, West Bengal, India*

**Alex Vitkin**

*Division of Biophysics and Bioimaging, Ontario Cancer Institute; Department of Medical Biophysics and Radiation Oncology, University of Toronto, 610 University Avenue, Toronto, Ontario M5G 2M9, Canada*



Studies of polarization properties of scattered light from turbid materials such as biological tissues have received considerable recent attention, because of the potential of polarimetric approaches for tissue imaging, characterization, and diagnosis. Polarization can be used as an effective tool to discriminate against multiply scattered light (acting as a gating / contrast mechanism) and thus may facilitate enhancement of contrast and resolution in tissue imaging. Moreover, the intrinsic tissue polarimetry characteristics contain wealth of morphological and functional information, which can be exploited for quantitative tissue characterization and assessment. However, in a complex random medium like tissue, numerous complexities due to multiple scattering and spatially inhomogeneous birefringence, as well as simultaneous occurrences of several polarization events, present formidable challenges for biomedical tissue polarimetry. In this chapter, we discuss advances in polarized light methodologies to overcome some of these challenges, and present illustrative examples of biomedical applications. Specifically, we review the basic polarimetry formalisms, outline the specific issues in tissue polarimetry, discuss the Stokes and Mueller experimental systems, and describe forward modeling of polarized light propagation in tissue. We then focus on inverse analysis for polarimetric results quantification and applications to quantitative tissue assessment. The other classes of polar-

ization applications in biomedicine, that of tissue imaging and polarization microscopy, are also mentioned in passing, with sufficient references to corresponding recent reviews of these topics.
**Key words:** polarization, multiple scattering, retardance and birefringence, turbid polarimetry, Monte Carlo simulations, Stokes vector, Mueller matrix, polar decomposition, tissue anisotropy, biological and medical applications

## 13.1 Introduction

Polarization of light has not been exploited to its full extend in biomedicine, partly because of the highly depolarizing nature of most biological tissues. This is unfortunate, because polarization offers an interesting contrast mechanism for tissue imaging and a rich abundance of important biophysical information of potential relevance to tissue diagnosis and characterization. Its partial neglect in biomedicine is slowly being redressed, however, as better experimental techniques of partial polarization detection and quantification, improved models of polarized light-tissue interactions, and refined interpretation of tissue polarization data, are emerging. As such, several attractive applications of this improved polarimetric methodology become feasible. In this chapter, we review polarized light fundamentals and mathematical formulations of polarized light propagation in biological tissues, describe forward and inverse problems in polarimetry of turbid media, discuss advances in various emerging polarimetric measurement systems, and focus on applications related to tissue diagnosis and assessment.

## 13.2 Fundamentals of Polarization

The definitions and properties of polarized light have been discussed at length in literature [1, 2, 3, 4], and so only a brief overview is provided here. In its classical description, polarization is a consequence of electromagnetic (EM) wave nature of light, in which the transverse oscillations of the electric and magnetic field vectors ($\vec{E}$ and $\vec{B}$) trace out stationary curves. If these vectors instead follow random paths in their temporal evolution, the resulting light is said to be unpolarized. The shape of the function traced out by the vectors defines the polarization state of the beam in question.

### 13.2.1 Polarization states

When the electric field vector $\vec{E}$ of an EM wave is confined to a plane, the resulting light is said to be linearly polarized, and when temporal evolution of the $\vec{E}$ vector traces out circles normal to the direction of the wave's propagation, the resulting beam is called circularly polarized. Linear and circular polarization are special cases of the more general elliptical polarization, in which $\vec{E}$ follows an ellipse as the wave propagates.

In the quantized description of polarization, each individual photon is polarized, and its associated state vector corresponds to one of the classical polarized states [5, 6]. When a large number of photons are considered, their collective behaviour is consistent with the classical limit (the wave solution to Maxwell's equations), and in the case when all of the photons in a beam of light exhibit the same polarization, the light is said to be fully polarized. On the other hand, when there are photons of different polarizations, but with a distribution favouring one particular state, the light is called partially polarized. Finally, when the photons are uniformly distributed over all possible

polarization states the light is said to be unpolarized. A useful quantification of this distribution is the degree of polarization, which measures of the uniformity, or lack thereof, of photon polarizations in a beam: the degree of polarization of fully polarized light is 1, and that of unpolarized light is 0. Depending on the magnitude of the relative surplus of a particular polarization state, a partially polarized beam of light can fall somewhere between these two extremes.

There are two mathematical formalisms commonly used to describe polarization: the Jones calculus [3, 5, 6], a field-based model which assumes coherent addition of the phase and amplitude of EM waves, and Stokes-Mueller calculus [3, 5, 6, 7, 8, 9], an intensity-based model which instead utilized incoherent addition of intensities. While theoretically interesting, the Jones formalism is limited in that it can describe pure polarization states, and it is thus ill suited for applications in which it is necessary to consider partial polarization. In general, biological tissues tend to be depolarizing, and so Jones calculus is rarely used in tissue polarimetry. Fortunately, the Stokes-Mueller formalism is capable of fully describing polarized light and its interaction with arbitrary materials, and so it is the mathematical system of choice in biomedical polarimetry.

### 13.2.2 Stokes-Mueller formalism

In this experimentally oriented formalism, polarization states are described by four measurable quantities, known as the Stokes parameters (introduced by G. G. Stokes in 1852). The four parameters, denoted $I$, $Q$, $U$, and $V$, are defined relative to six different intensity measurements, each corresponding to the intensity of a beam in question after it has passed through various ideal polarizers: $I_H$ is the intensity through a horizontal linear polarizer, $I_V$ through a vertical linear polarizer, $I_P$ and $I_M$ through linear polarizers at $45^\circ$ and $135^\circ$ (or $-45^\circ$) respectively, and finally $I_R$ and $I_L$ through right and left circular polarizers, respectively. The Stokes parameters are often combined into a four dimensional vector, called a Stokes vector, in which the parameters can be written as

$$S = \begin{bmatrix} I \\ Q \\ U \\ V \end{bmatrix} = \begin{bmatrix} I_H + I_V \\ I_H - I_V \\ I_P - I_M \\ I_R - I_L \end{bmatrix}. \tag{13.1}$$

Thus, $I$ represents the total intensity of the light, $Q$ and $U$ represent the degree and orientation of linear polarization, and $V$ represents the degree and direction of circular polarization. Note that $I$ is given above as a sum of horizontal and vertical polarized intensities, even though a sum of any two orthogonal polarization states would do; also note that S is not a vector in the classical sense (not a directional quality), but in the column-matrix sense of the word. The Stokes parameters are related by

$$I^2 \geq Q^2 + U^2 + V^2, \tag{13.2}$$

where the equality holds in the case of full polarization, and the inequality for partial polarization. Thus, the degree of polarization is defined as a function of the Stokes parameters by

$$DOP = \frac{\sqrt{Q^2 + U^2 + V^2}}{I}, \tag{13.3}$$

so when a beam is unpolarized ($DOP = 0$), we have that $Q = U = V = 0$. Further, the degree of linear polarization is defined by

$$DOLP = \frac{\sqrt{Q^2 + U^2}}{I}, \tag{13.4}$$

and the degree of circular polarization by

$$DOCP = \frac{V}{I}. \tag{13.5}$$

When light described by the Stokes vector $S_{in}$ interacts with a material, its polarization state is usually modified, and the resulting light can be described by the Stokes vector $S_{out}$. The transfer function between the input and output states can be written as a linear equation

$$S_{out} = \mathbf{M}S_{in}, \tag{13.6}$$

where $\mathbf{M}$ is a $4 \times 4$ matrix known as a Mueller matrix (named after its inventor Hans Mueller, who introduced it in the 1940s). Expanding Eq. (13.6) into its components gives

$$\begin{bmatrix} I_{out} \\ Q_{out} \\ U_{out} \\ V_{out} \end{bmatrix} = \begin{bmatrix} M_{1,1} & M_{1,2} & M_{1,3} & M_{1,4} \\ M_{2,1} & M_{2,2} & M_{2,3} & M_{2,4} \\ M_{3,1} & M_{3,2} & M_{3,3} & M_{3,4} \\ M_{4,1} & M_{4,2} & M_{4,3} & M_{4,4} \end{bmatrix} \begin{bmatrix} I_{in} \\ Q_{in} \\ U_{in} \\ V_{in} \end{bmatrix}. \tag{13.7}$$

The effects of a material on polarized light are completely described by its corresponding Mueller matrix [3, 6, 9], and so the matrix's 16 elements (15 if the change in absolute intensity is excluded) serve as the sample's 'polarization fingerprint', from which it is possible to infer information about its physical nature.

It is important to note that not every real $4 \times 4$ matrix is a physically realizable Mueller matrix. The fundamental requirement for these matrices is that they map to a physically significant Stokes vector (i.e., one satisfying Eq. (13.2)) for every possible incident polarization state [8, 9].

While both the Jones and the Stokes-Mueller formalisms describe polarization change using matrix/vector equations, the later provides a framework with which depolarizing materials (e.g., biological samples) can be described. So while the $2 \times 2$ transfer matrices of Jones calculus can potentially be useful theoretical tool, their practical applications have been limited to describing specular reflections, clear media, and thin films where depolarization is not an issue. Mueller matrices, on the other hand, not only provide a complete description of a much wider range of physical materials, but their elements are associated with various intensities (rather than amplitudes), and so they can be experimentally determined with relative ease using intensity-measuring conventional (square-law detector) instruments, such as polarimeters, spectrometers and radiometers. Thus, for the purposes of this chapter, we will employ the Stokes-Mueller formalism exclusively for describing biomedical polarimetry.

### 13.2.3 Fundamental polarimetric characteristics

There are three principle characteristics of interest that a Mueller matrix can encode: depolarization, diattenuation and retardance, all of which will be examined in further detail.

#### 13.2.3.1 Depolarization

If the degree of polarization of a beam incident on a sample is equal to $m$ (where $m$ is between 0 and 1), and the light resulting from the interaction has a degree of polarization $n$, where $m > n$, then the sample is said to be depolarizing. For the incident beam

$$m = \frac{\sqrt{Q_{in}^2 + U_{in}^2 + V_{in}^2}}{I}, \tag{13.8}$$

and so in the case that the intensity is unchanged, the degree of polarization of the resulting light can be written as

$$n = \frac{\sqrt{Q_{out}^2 + U_{out}^2 + V_{out}^2}}{I} = \frac{\sqrt{(aQ_{in})^2 + (bU_{in})^2 + (cQ_{in})^2}}{I}, \tag{13.9}$$

where $|a|,\ |b|,\ |c| \leq 1$. This relation can be cast in matrix form (like that of Eq. (13.6)) by taking the Mueller matrix of the sample to be [8, 10]

$$\mathbf{M}_\Delta = \begin{bmatrix} 1 & 0 & 0 & 0 \\ 0 & a & 0 & 0 \\ 0 & 0 & b & 0 \\ 0 & 0 & 0 & c \end{bmatrix} \quad |a|,\ |b|,\ |c| \leq 1 \tag{13.10}$$

Thus, $1-|a|$ and $1-|b|$ are the linear depolarization factors (for horizontal/vertical and $\pm 45^\circ$ respectively), and $1-|c|$ is the circular depolarization factor. The net depolarization, denoted $\Delta$, is usually defined as

$$\Delta = 1 - \frac{|a|+|b|+|c|}{3} = 1 - \frac{|Tr(\mathbf{M}_\Delta)-1|}{3}, \tag{13.11}$$

so $\Delta$ remains between 0 and 1.

Note that this *depolarization factor of the medium* is not the same as the various Stokes degrees of polarization in Eqs. (13.3)–(13.5). The later quantify the amount of *polarization of the light beam*, whereas the former describes the tendency of a material to depolarize light, in a manner that is somewhat independent of the polarization state of the incident light. In general, the two quantities can be approximately related as $DOP_{light} \sim 1 - \Delta_{medium}$, although this relation only holds as an equality in special cases. In biomedical polarimetry, the dominant processes causing depolarization are multiple scattering and spatially heterogeneous arrangements of uniaxially birefringent domains. A material with a large value of $\Delta$ is significantly depolarizing, and so in general, the degree of polarization of light after interaction with such a medium will tend to be low.

#### 13.2.3.2 Diattenuation

The following two polarization effects, namely diattenuation and retardance, are both the result of differences in the refractive indices for different polarization states, and are often described in terms of ordinary and extraordinary axis and indices. Differences in the real parts of said indices result in linear and circular birefringence (retardance), whereas differences in the imaginary parts can cause linear and circular dichroism (which manifests itself as diattenuation). Diattenuation is analogous to dichroism, which is the differential absorption of two orthogonal polarization states (linear or circular); however, diattenuation is more general, since the differential attenuation need not be caused by absorption, but rather, it can be the result of various other effects (e.g, scattering).

The diattenuation ($d$) of an optical element is a measure of the differential attenuation of orthogonal polarization states, for both linear and circular polarization. Thus, linear diattenuation is defined as the differential attenuation of two orthogonal linear polarization states (e.g., $\pm 45^\circ$), and circular diattenuation is defined as the differential attenuation of right and left circular polarization states. The Mueller matrix of an ideal diattenuator can be defined using three parameters: $q$ and $r$, the intensity transmittance (or reflectance) of the two incident orthogonal polarization states in question (be they linear or circular), and $\theta$, the angle (with respect to the horizontal) at which the principle axis is oriented. For a linear diattenuation, the Mueller matrix is defined as [8, 10]

$$\begin{bmatrix} q+r & (q-r)\cos(2\theta) & (q-r)\sin(2\theta) & 0 \\ (q-r)\cos(2\theta) & (q+r)\cos^2(2\theta)+2\sqrt{qr}\sin^2(2\theta) & (q+r-2\sqrt{qr}\sin(2\theta)\cos(2\theta) & 0 \\ (q-r)\sin(2\theta) & (q+r-2\sqrt{qr}\sin(2\theta)\cos(2\theta) & (q+r)\cos^2(2\theta)+2\sqrt{qr}\sin^2(2\theta) & 0 \\ 0 & 0 & 0 & 2\sqrt{qr} \end{bmatrix}. \tag{13.12}$$

In the circular case, the dependence on $\theta$ disappears due to rotational symmetry, and so the general

Mueller matrix for a circular diattenuator is [8, 10]

$$\mathbf{M}_{\mathrm{D}} = \begin{bmatrix} q+r & 0 & 0 & q-r \\ 0 & 2\sqrt{qr} & 0 & 0 \\ 0 & 0 & \sqrt{qr} & 0 \\ q-r & 0 & 0 & q+r \end{bmatrix}. \tag{13.13}$$

A common example of a diattenuator is an ideal polarizer, which can transform an unpolarized incident beam to fully polarized light ($d = 1$ in this case), albeit often with a significant decrease in the intensity $I$.

#### 13.2.3.3 Retardance (birefringence)

Retardance, closely related to birefringence, is the property in which a material introduces a phase shift between two orthogonal polarization states when it interacts with incident light. Mathematically, the two are related simply via $\delta = kL\Delta n$, where $\delta$ is the retardance, $k$ is the wave vector of the light, $L$ is the pathlength in the medium, and $\Delta n$ is the difference in the real parts of the refractive index known as birefringence. Linear retardance (or linear birefringence), denoted $\delta$, takes place between linear polarization components separated by a geometric angle of 90° (e.g., horizontal and vertical linear polarization components). Note that linear birefringence (retardance) is a vector quantity, possessing both a magnitude and a direction (orientation). The general Mueller matrix of a pure linear retarder with retardance $\delta$ and a fast axis oriented at an angle $\theta$ is [8, 10]

$$\begin{bmatrix} 1 & 0 & 0 & 0 \\ 0 & \cos^2(2\theta)+\sin^2(2\theta)\cos(\delta) & \sin(2\theta)\cos(2\theta)\,[1-\cos(\delta)\,] & -\sin(2\theta)\sin(\delta) \\ 0 & \sin(2\theta)\cos(2\theta)\,[1-\cos(\delta)\,] & \sin^2(2\theta)+\cos^2(2\theta)\cos(\delta) & \cos(2\theta)\sin(\delta) \\ 0 & \sin(2\theta)\sin(\delta) & -\cos(2\theta)\sin(\delta) & \cos(\delta) \end{bmatrix} \tag{13.14}$$

Circular retardance (optical rotation), denoted $\psi$, arises from phase differences between right circularly polarized (RCP) and left circularly polarized (LCP) states. The Mueller matrix of a circular retarder with an optical rotation of $\psi$ is [8, 10]

$$\begin{bmatrix} 1 & 0 & 0 & 0 \\ 0 & \cos(2\psi) & -\sin(2\psi) & 0 \\ 0 & \sin(2\psi) & \cos(2\psi) & 0 \\ 0 & 0 & 0 & 1 \end{bmatrix} \tag{13.15}$$

## 13.3 Experimental Polarimetry

There are two principle applications in biomedical polarimetry research: tissue imaging and tissue characterization. Both of these require highly accurate measurements of the polarization retaining signals, as biological tissues tend to be strongly depolarizing due to multiple scattering and/or birefringence domains of varying magnitude and orientation, thus creating a large depolarized source of noise which can inhibit the detection of the weak remaining information-carrying polarization signal. Thus, many traditional polarimetry systems (e.g., crossed linear polarizers used in microscopy for examining thin fixed *ex-vivo* tissue slices) are poorly suited for these applications.

Polarimetric approaches offer an additional contrast mechanism that confers two main advantages over intensity-only polarization-insensitive methods: they allow for some discrimination against multiply scattered light, which can enable higher resolution imaging of tissues and their underlying

structures [11], and they provide a method for non-invasive and quantitative tissue diagnosis, since the polarimetric characteristics of tissues can encode a large amount of biochemical, morphological, and functional information [12, 13, 14]. A variety of experimental tools for exploiting these advantages have been developed, which are capable of performing reliable measurements of polarimetric tissue data, despite the aforementioned technical and biophysical challenges. Such instruments can be used to measure the Stokes vector of a beam upon interacting with the sample in question, and/or the Mueller matrix of the sample itself.

### 13.3.1 Stokes polarimeters

As discussed in Section 13.2.2, the Stokes parameters corresponding to a beam of light can be determined by performing six intensity measurements through linear and circular polarizers ($I_H$, $I_V$, $I_P$, $I_M$, $I_R$, $I_L$) [9]. By exploiting the property that $I_H + I_V = I_P + I_M = I_L + I_R$, it is possible to determine the Stokes parameters of a beam with only four measurements, using a linear polarizer, with transmission axis aligned at $+45^\circ$ above the horizontal axis, followed by a quarter wave plate, with its fast axis oriented horizontally. Combined, these two elements form a circular polarizer. Three sets of intensity measurements (denoted $I_{cir}(\alpha)$, where $\alpha$ is the angle of the combined polarizer's fast axis above the horizontal) are performed by varying the angle ($\alpha$) of the circular polarizer with respect to the horizontal axis. The first three measurements are at $\alpha = 0^\circ$, $45^\circ$, and $90^\circ$, and the final measurement, denoted $I_{lin}(\alpha)$ is performed by turning the combined polarizer around and setting $\alpha$ to $0^\circ$. The Stokes parameters can be inferred from these intensity measurements by

$$\begin{bmatrix} I \\ Q \\ U \\ V \end{bmatrix} = \begin{bmatrix} I_{cir}(0^\circ) + I_{cir}(90^\circ) \\ I - 2I_{cir}(45^\circ) \\ I_{cir}(0^\circ) - I_{cir}(90^\circ) \\ -I + 2I_{lin}(0^\circ) \end{bmatrix}. \tag{13.16}$$

This measurement scheme, first proposed by Collett [15], has been used to measure the Stokes parameters of transmitted (or backscattered) light from tissue and tissue-like turbid media [16, 17, 18, 19, 20]. However, in order to accurately quantify tissue polarimetric characteristics, it is generally desirable to use a more sensitive detection method.

One method that shows promise in performing measurements with in the challenging biomedical environment is the use of polarization modulation with synchronous detection. Various sensitive detection schemes are possible with this approach; some perform polarization modulation on the beam that is incident on the sample, whereas others modulate the sample-emerging light by placing the polarization modulator between the sample and the detector. The resulting periodic signal can be synchronously monitored with a phase-sensitive (lock-in amplifier based) detection method, and then analyzed to extract the polarization properties of the beam (Stokes polarimetry) or of the sample (Mueller polarimetry) that are linked to the physical quantities of interest.

A schematic diagram of one particular polarimeter employing polarization modulation and synchronous lock-in amplification is shown in Fig. 13.1.1 [21]. The system is seeded with unpolarized light from the laser, which then passes through a mechanical chopper operating at a low frequency $f_c$ (typically in the tens-hundreds of Hz range, exact value unimportant). The chopper is used in conjunction with lock-in detection to accurately establish the overall signal intensity ($I$), while eliminating the contributions of the output or background fluctuations and any dark current. The input optics, comprised of a linear polarizer ($P_1$) and an orientation-adjustable quarter wave plate ($QWP_1$) enable the generation of any input polarization state (with $DOP = 1$). Following the light-tissue interactions, the beam enters the detection optics, which consist of a removable quarter wave plate ($QWP_2$), with its fast axis oriented at $-45^\circ$, followed by a photoelastic modulator (PEM), a linearly birefringent resonant device operating in the kilohertz range (e.g. $f_p \sim 50$ kHz), whose fast axis is horizontal ($0^\circ$) and whose retardation ($\delta_{PEM}$) is modulated sinusoidally according to the function $\delta_{PEM}(t) = \delta_o \sin(\omega t)$, where $\omega = 2\pi f_p$ and $\delta_o$ is the PEM's user-specific amplitude of maximum

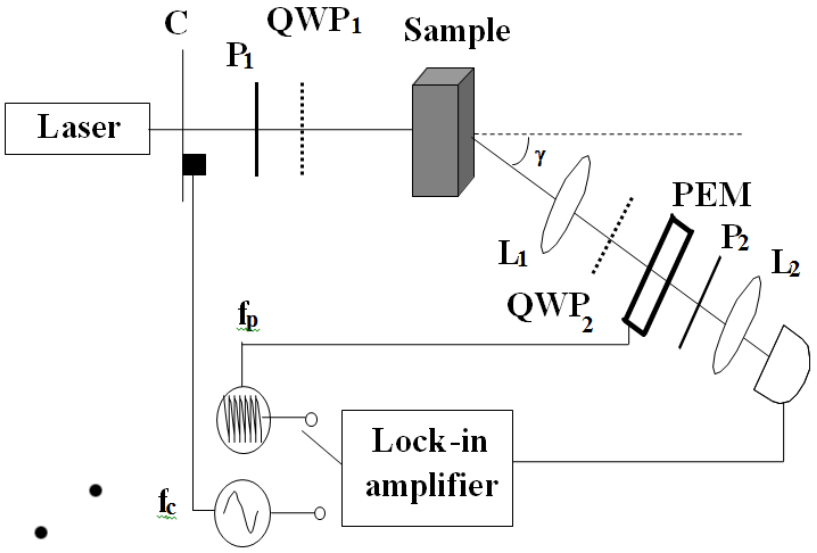


**Figure 13.1:** A polarimeter employing polarization modulation and synchronous detection to measure Stokes parameters. $C_1$ is a mechanical chopper, $P_1$ and $P_2$ are linear polarizers, $QWP_1$ and $QWP_2$ are removable quarter wave plates, $L_1$ and $L_2$ are lenses, PEM is a photoelastic modulator, and APD a photodetector. The chopper and the PEM modulate the signal with frequencies $f_c$ and $f_p$ respectively. The detection optics can be rotated by an angle $\gamma$ around the sample (Adopted from [13]).

retardation. When measuring the Stokes parameters $Q$ and $U$, the fast axis of $QWP_2$ is oriented at $-45°$, and when measuring $V$, said retarder is removed altogether. The PEM is followed by a linear polarizer (referred to as an analyzer) oriented at 45°, which converts the polarization modulation from the PEM into intensity modulation suitable for photodetection. The resulting light is collected using a pair of lenses, and focused onto a photodetector (e.g., an avalanche photodiode), the signal from which is sent to a lock-in amplifier. In order to extract the Stokes parameters from the alternating photocurrent, the reference input of the lock-in amplifier is toggled between the chopper frequency ($f_c$) and the PEM modulation frequency ($f_p$) and its harmonics.

In this experimental arrangement, the Stokes vector of the beam entering the detector, denoted $S_f = \begin{bmatrix} I_f & Q_f & U_f & V_f \end{bmatrix}^T$, can be related to that of the sample-emerging light, denoted $S = \begin{bmatrix} I & Q & U & V \end{bmatrix}^T$, by multiplying the vector representing the input state by the Mueller matrices of the optical elements [21]. When the $QWP_2$ is in place, the relation is

$$\begin{bmatrix} I_f \\ Q_f \\ U_f \\ V_f \end{bmatrix} = \frac{1}{2} \begin{bmatrix} 1 & 0 & 1 & 0 \\ 0 & 0 & 0 & 0 \\ 1 & 0 & 1 & 0 \\ 0 & 0 & 0 & 0 \end{bmatrix} \begin{bmatrix} 1 & 0 & 0 & 0 \\ 0 & 1 & 0 & 0 \\ 0 & 0 & \cos(\delta) & \sin(\delta) \\ 0 & 0 & -\sin(\delta) & \cos(\delta) \end{bmatrix} \begin{bmatrix} 1 & 0 & 0 & 0 \\ 0 & 0 & 0 & 1 \\ 0 & 0 & 1 & 0 \\ 0 & -1 & 0 & 0 \end{bmatrix} \begin{bmatrix} I \\ Q \\ U \\ V \end{bmatrix}, \tag{13.17}$$

and when $QWP_2$ is removed it is

$$\begin{bmatrix} I_{fr} \\ Q_{fr} \\ U_{fr} \\ V_{fr} \end{bmatrix} = \frac{1}{2} \begin{bmatrix} 1 & 0 & 1 & 0 \\ 0 & 0 & 0 & 0 \\ 1 & 0 & 1 & 0 \\ 0 & 0 & 0 & 0 \end{bmatrix} \begin{bmatrix} 1 & 0 & 0 & 0 \\ 0 & 1 & 0 & 0 \\ 0 & 0 & \cos(\delta) & \sin(\delta) \\ 0 & 0 & -\sin(\delta) & \cos(\delta) \end{bmatrix} \begin{bmatrix} I \\ Q \\ U \\ V \end{bmatrix}. \tag{13.18}$$

Thus, the intensity measured by the photodetector is

$$I_f = \frac{I}{2}[1 - q\sin\delta_{PEM} + u\cos\delta_{PEM}], \tag{13.19}$$

with $QWP_2$ in place, and

$$I_{fr} = \frac{I}{2}[1 - v\sin\delta_{PEM} + u\cos\delta_{PEM}], \tag{13.20}$$

when it is removed. Here $q$, $u$, and $v$ are the normalized polarization parameters, defined as $q = Q/I$, $u = U/I$, and $v = V/I$. These parameters can be recovered from $I_f$ and $I_{fr}$ by expressing Eqs. (13.19) and (13.20) as Fourier series whose coefficients are given by Bessel functions (this follows since a periodic function whose argument is itself periodic is represented as a series of harmonics with Bessel coefficients [22]). By setting the peak modulation retardance to $\delta_o = 2.405$ radians (corresponding to the first root of the zeroth-order Bessel function), the normalized polarization parameters can be expressed as functions of the synchronously-detected signals at the chopper frequency $V_{f_c}$, as well as the first and second harmonics of the photoelastic modulation frequency, $V_{f_{PEM}}$ and $V_{2f_{PEM}}$ respectively. When the detection wave plate is in place, we have [21]

$$q = \frac{V_{f_{PEM}}}{V_{f_c}\sqrt{2}\,J_1(\delta_o)}, \tag{13.21}$$

$$u = \frac{V_{2f_{PEM}}}{V_{f_c}\sqrt{2}\,J_2(\delta_o)}, \tag{13.22}$$

and with $QWP_2$ removed:

$$v = \frac{V_{f_{PEM}}}{V_{f_c}\sqrt{2}\,J_1(\delta_o)}. \tag{13.23}$$

Thus, the synchronous lock-in detected signals recovered at the first and second harmonics of the polarization modulation frequency, along with that at the chopper frequency, can be used to determine the Stokes parameters of a beam with high SNR for any given state of polarization [21].

While this single PEM scheme is faster and more accurate than sequential DC measurements, it does not allow one to measure all four Stokes parameters simultaneously, as the measurement of circular polarization requires the manual addition of a wave plate in the beam path, making it difficult to automate measurements, and rendering the method inaccurate for time-varying Stokes vectors. Fortunately, the system described above has been generalized to include a second photoelastic modulator (placed directly after the first), which allows for the quasi-simultaneous automated measurement of the complete Stokes vectors with a high SNR [23]. The second PEM removes the need for a quarter wave plate, as the bi-periodic intensity oscillations produced by the dual PEMs along with the linear polarizer contain sufficient information to fully describe the polarization state of the beam in question. Such a system has proven to be useful as it allows for rapid and flexible measurement of Stokes vectors, which is useful in itself, and/or can be processed further to enable Mueller polarimetry.

### 13.3.2 Mueller Polarimeters

While knowing the Stokes vector of a beam after it has interacted with a sample can be very informative, this information is dependent on sample properties *and* on the input light beam (as evident from Eq. (13.6)). Thus, it is often desirable to determine the sample's Mueller matrix itself, which provides a comprehensive description of its polarimetric properties independent of incident light polarization (its true polarization transfer function). Devices capable of performing such measurements, known as Mueller matrix polarimeters, have successfully used both DC (using sequential static measurements) and AC polarization modulation techniques.

The central difference between Stokes and Mueller experimental polarimetry is that the later requires knowledge of the polarimetric state of a beam both before and after its interaction with the sample. In general, it is necessary to know at least 16 independent polarization parameters for both the input and the output states [1, 3, 8]. That is, if one knows the Stokes vectors of at least four (suitably selected) input beams before they interact with the sample and then after they do so, then it is possible to determine the transfer function (the Mueller matrix) of the material in question. In general, if $S_{in}^i$ is the Stokes vector corresponding to the $i$-th input beam and $S_{out}^i$ is that of the corresponding output state, then the two vectors can be related as

$$S_{out}^i = \mathbf{M} S_{in}^i \tag{13.24}$$

If the input and output vectors are known for $n$ beams (i.e., $1 \leq i \leq n$), then each input/output pair can be related using Eq. (13.24). The resulting $n$ linear equations can be combined in matrix form as

$$\left[ S_{out}^1 \cdots S_{out}^n \right] = \left[ \mathbf{M} S_{in}^1 \cdots \mathbf{M} S_{in}^n \right] = \mathbf{M} \left[ S_{in}^1 \cdots S_{in}^n \right], \tag{13.25}$$

and so the sample Mueller matrix is given by

$$\mathbf{M} = \left[ S_{out}^1 \cdots S_{out}^n \right] \left[ S_{in}^1 \cdots S_{in}^n \right]^{-1}, \tag{13.26}$$

provided $\left[ S_{in}^1 \cdots S_{in}^n \right]$ is invertible (so $n$ must equal 4). In practice, the invertability of a matrix is not binary (i.e., either invertible or not), but rather presents a continuum in which some matrices are more invertible than others. Given the imperfect nature of experimental measurements, a matrix ill-suited for inversion (known as poorly-conditioned) will tend to amplify Stokes measurement errors into the determined Mueller matrix, whereas a well-conditioned matrix will minimize their impact. Several authors have addressed the issue of robust Mueller polarimetry based on optimum selection of input Stokes states [24, 25, 26]; some results from a recent study by Layden et al. [27] are summarized here. In Mueller polarimetry, a globally well-conditioned matrix $\left[ S_{in}^1 \cdots S_{in}^n \right]$ is one whose Stokes vectors (columns) are evenly distributed over the Poincaré sphere [28]. It is possible, and sometimes advantageous, to generalize Eq. (13.26) to the case of $n \geq 4$ by replacing the traditional inverse with the Moore-Penrose pseudoinverse defined as

$$\mathbf{A}^+ = \mathbf{A}^T (\mathbf{A}\mathbf{A}^T)^{-1}, \tag{13.27}$$

where $\mathbf{A}^+$ is said to be the pseudoinverse of the matrix $\mathbf{A}$. In order to quantify the robustness of a Mueller matrix determined from a given set of input Stokes vectors (and their corresponding output vectors), one can perturb the elements in Eq. (13.26) by incorporating measurement errors. Thus, each Stokes vector $S^i$ becomes $S^i + \delta S^i$, where $\delta S^i$ represents the measurement error associated with the given polarization state. Naturally, the measurement errors in these vectors propagate into the inferred Mueller matrix, which takes the form

$$\mathbf{M} + \delta\mathbf{M} = \left[ S_{out}^1 + \delta S_{out}^1 \cdots S_{out}^n + \delta S_{out}^n \right] \left[ S_{in}^1 + \delta S_{in}^1 \cdots S_{in}^n + \delta S_{in}^n \right]^+, \tag{13.28}$$

where $\delta\mathbf{M}$ is the $4 \times 4$ matrix representing the deviation from the sample's true transfer function. To maximize the robustness of such a polarimeter, the root mean square of the error $\delta\mathbf{M}$ can be minimized by choosing input Stokes vectors which form the vertices of Platonic solids on the Poincaré sphere [27].

The polarization modulation experimental setups described in Section 13.3.1 can be used to measure the Mueller matrix of a sample by first selecting at least 4 different polarization state generator configurations and measuring their resulting Stokes vectors, and then by sequentially shining those same beams onto a sample, and measuring the corresponding Stokes vectors of the resulting light. This approach has been used in complex tissue-like turbid media and in actual tissues [29, 30] and some of the representative results are presented in Section 13.6. Different Mueller polarimeters

employing photoelastic modulators have been explored, some of which modulate not only the light emerging from the sample, but also the original beam, before it is incident on the material of interest. Thus, by putting the sample between two or more PEMs, it can be possible to monitor the various modulation frequencies (and their harmonics) to directly recover the elements of the sample Mueller matrix, while bypassing Stokes vector measurements altogether.

Another type of modulation-based Mueller polarimeter involves the use of dual rotating retarders. In this approach, which has been widely used in tissue polarimetry [31, 32, 33], the polarization of the sample-incident light is modulated by passing a beam through a fixed linear polarizer, followed a wave plate (with retardation $\delta_1$) rotating at an angular velocity of $\omega_1$. This beam is then incident on the sample, and the resulting light is directed through the analyzing optics, which consist of another rotating wave plate (with retardation $\delta_2$, rotating at angular velocity $\omega_2$) and a linear polarizer, which is held fixed. The rotation of the two wave plates results in a periodic variation in the measured intensity, which can be analyzed by multiplying the Mueller matrices corresponding to the elements in the optical path (i.e., the polarizers, wave plates, and the sample). In the most common configurations, the axes of the polarizers are set parallel, the wave plates are both chosen to have a quarter wave retardance ($\delta_1 = \delta_2 = \frac{\pi}{2}$) and their angular velocities are set at a 5:1 ratio ($5\omega_1 = \omega_2$) [31, 33]. It has been shown that this ratio of angular velocities allows for the recovery of all sixteen Mueller matrix elements from the amplitudes and phases of the twelve frequencies in the intensity signal. In order to compute these elements, the detected signal is Fourier analyzed, and the elements of the Mueller matrix can be inferred from the resulting coefficients. A more generalized version of this measurement scheme could use arbitrary values of retardation and polarizer orientations, as well as a different ratio of angular velocities, in order to determine prioritized Mueller matrix elements with greater precision and/or higher SNR [31, 33].

Another noteworthy polarimetric measurement scheme that employs polarization modulation is the snapshot Mueller matrix polarimeter [34]. This measurement method encodes polarimetric information in different wavelengths of a beam, allowing for highly sensitive and instantaneous measurement of all sixteen Mueller matrix elements simultaneously. To do so, a broadband spectrum source is used in conjunction with two birefringent retarders and a linear polarizer to produce the incident beam, and the light emerging from the sample is analyzed using a similar combination of birefringent retarders and a linear polarizer. The thickness of the retarders on either side of the sample are optimized to recover and analyze sufficiently many polarization states, and the resulting spectral signals (over a narrow range of $\Delta\lambda \sim 10$nm), which are recorded using a spectrometer, are Fourier analyzed to produce all sixteen Mueller matrix elements.

While modulation based Mueller polarimeters show great promise in point measurements, they usually involve synchronous detection, which can make them poorly suited for imaging larger areas. Instead, such measurements are usually performed with DC-based polarimeters, by sequentially measuring the intensities with at least sixteen different configurations of source polarizers and detection analyzers [35]. Unfortunately, such an approach results in fairly low sensitivity measurements, and alternative methods have been investigated. One such method involves liquid crystal variable retarders, which enables the measurement of Mueller matrices with higher sensitivity and precision [36, 37, 38]. Such a polarimeter is comprised of a polarization state generator (PSG) unit, a polarization state analyzer (PSA) unit and an imaging camera, for spatially resolved signal detection. The PSG, which polarizes the light incident on the sample, is composed of a linear polarizer ($P_1$) and two liquid crystal variable retarders ($LC_1$ and $LC_2$), with adjustable retardances of $\delta_1$ and $\delta_2$ respectively, whose birefringent axes are aligned at angles $\theta_1$ and $\theta_2$ with the axis of the polarizer [37]. A schematic of such a measurement scheme is shown in Fig. 13.2.

One widely used configuration involves setting $\theta_1 = 45^\circ$ and $\theta_2 = 0^\circ$, in which case the Stokes vector, $S_{in}$, of the light incident on the sample can be expressed as a simple function of the retar-

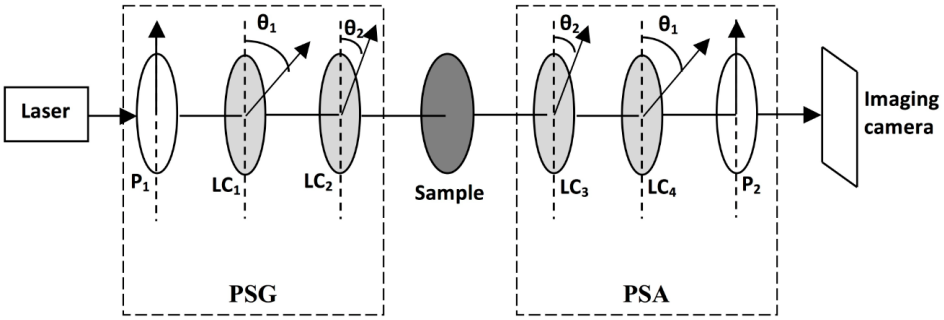


**Figure 13.2:** A liquid crystal variable retarder polarimeter, where $P_1$ and $P_2$ are linear polarizers, and $LC_1$–$LC_4$ are liquid crystal variable retarders. Together, $P_1$, $LC_1$ (having retardance of $\delta_1$ and orientation angle $\theta_1$), and $LC_2$ (having retardance of $\delta_2$ and orientation angle $\theta_2$) comprise the polarization state generator (PSG). Likewise, $LC_3$ (having retardance of $\delta_2$ and orientation angle $\theta_2$), $LC_4$ (having retardance of $\delta_1$ and orientation angle $\theta_1$), and $P_2$ collectively form the polarization state analyzer (PSA). While the above schematic depicts transmission measurements, other detection geometries are possible using this measurement scheme.

dances [38]

$$S_{in} = \begin{bmatrix} 1 & 0 & 0 & 0 \\ 0 & 1 & 0 & 0 \\ 0 & 0 & \cos\,\delta_2 & \sin\,\delta_2 \\ 0 & 0 & -\sin\,\delta_2 & \cos\,\delta_2 \end{bmatrix} \begin{bmatrix} 1 & 0 & 0 & 0 \\ 0 & \cos\,\delta_1 & 0 & -\sin\,\delta_1 \\ 0 & 0 & 1 & 0 \\ 0 & \sin\,\delta_1 & 0 & \cos\,\delta_1 \end{bmatrix} \begin{bmatrix} 1 \\ 1 \\ 0 \\ 0 \end{bmatrix} = \begin{bmatrix} 1 \\ \cos\,\delta_1 \\ \sin\,\delta_1 \sin\delta_2 \\ \sin\,\delta_1 \cos\delta_2 \end{bmatrix} \tag{13.29}$$

It is apparent from Eq. (13.29) that any possible polarization state on the Poincaré sphere can be generated with the proper choice of $\delta_1$ and $\delta_2$. The system's PSA consists of a similar arrangement of liquid crystal variable retarders ($LC_3$ and $LC_4$) and a linear polarizer, but positioned in the reverse order with respect to the incoming light. It is followed by a detector, which, for imaging applications, is a CCD camera.

The PSG unit can be used to produce four unique Stokes vectors, which can be grouped into a $4 \times 4$ generator matrix $\mathbf{W}$, where the $i$-th column of $\mathbf{W}$ corresponds to the $i$-th polarization state. Similarly, after sample interactions, the PSA results can be described by a $4 \times 4$ analyzer matrix $\mathbf{A}$. The Stokes vectors of the light to be analyzed are projected onto four basis states, given by the rows of $\mathbf{A}$. The sixteen intensity measurements required for the construction of a full Mueller matrix are grouped into the measurement matrix $\mathbf{M}_i$, which can be related to PSA/PSG matrices $\mathbf{W}$ and $\mathbf{A}$, as well as the sample Mueller matrix $\mathbf{M}$ by [8, 39]

$$\mathbf{M}_i = \mathbf{A}\,\mathbf{M}\,\mathbf{W}. \tag{13.30}$$

The sample Mueller matrix can be represented as a 16 element column vector $M^{vec}$, which can be related to the corresponding $16 \times 1$ intensity measurement vector $M_i^{vec}$ as

$$M_i^{vec} = \mathbf{Q} M^{vec}, \tag{13.31}$$

where $\mathbf{Q}$ is the $16 \times 16$ matrix given by the Kronecker product of $\mathbf{A}$ with the transpose of $\mathbf{W}$:

$$\mathbf{Q} = \mathbf{A} \otimes \mathbf{W}^T \tag{13.32}$$

Once the exact forms of the system A and W matrices are known, all the sixteen elements of the sample Mueller matrix ($M^{vec}$, written in column vector form) can be determined from the sixteen

measurements ($M_i^{vec}$). The $4 \times 4$ sample Mueller matrix is obtained by rearranging the elements of $M^{vec}$. One important advantage of this approach is that, it allows for calibration and determination of the exact forms of the system PSG and PSA matrices [37]. This can be accomplished by the so-called "eigenvalue calibration method", wherein the exact forms of the system PSG (**W**) and PSA (**A**) matrices are determined from measurements on calibrating samples having known forms of Mueller matrices (e.g., a set of quarter wave plates and polarizers) [36, 37, 39]. As is apparent, several specific measurement schemes are possible under this general approach, depending on the selected values of $\delta_1$ and $\delta_2$, as well as $\theta_1$ and $\theta_2$. Several such configurations have therefore been examined, and some authors have determined the values of the system parameters (elements of **A** and **W** matrices), which optimize the polarimeter and minimize the noise in the resulting Mueller matrix, resulting in more accurate tissue measurements [36].

Recently, a modulation-based polarimetric imaging scheme employing stroboscopic illumination has been explored for large surface area measurements [40]. In this novel approach, the sample is illuminated by a laser, whose pulses are precisely controlled by a programmable pulse generator. The temporal reference is triggered by the controller of a photoelastic modulator (PEM) operating at 50 kHz, and the resulting synchronization facilitates "freezing" the intensity variation of the modulated signal at desirable temporal phases. The intensity is measured (with a CCD camera) at four specific temporal phases, which are made affectively static via stroboscopic illumination, and the resulting data is used to infer two-dimensional images of ellipsometric parameters [40, 41]. While this approach may hold promise, it has not yet been employed for complete (sixteen element) Mueller matrix imaging.

## 13.4 Forward Modeling of Polarization Transfer in Complex Random Media

Accurate modeling of interaction of polarized light with tissue micro-structures and its propagation through turbid tissue is extremely useful for the applications of polarized light methods for tissue imaging, characterization and diagnosis. The insight gained from such *forward models* helps in designing and optimizing experiments, and analyzing/interpreting measured data, for specific applications.

A rigorous, electromagnetic theory based approach for analyzing light propagation in tissue will need to identify and incorporate the spatio-temporal distribution of complex tissue dielectric structures (different cells and subcellular structures, connective stromal tissues / extra-cellular matrix, blood and lymphatic networks, interstitial fluids, etc.) and their absorption and scattering properties. Clearly this is a formidable task. Due to the ensuing complexity, heuristic approaches with different levels of approximations have been developed to model light transport in tissues. Radiative transport theory and its simplified variant, the diffusion equation, are often used to model light propagation in tissue [42, 43, 44]. However, both of these are intensity based (scalar) techniques, and typically neglect the vector nature of light (polarization). Some attempts have been made to use the vector radiative transfer equation (VRTE) in this framework to incorporate polarization information by describing transport of the Stokes vectors of light (photon packets) through a random medium [42, 44]. However, solving the VRTE in real systems is rather complex, and the solutions are often too slow and insufficiently flexible to handle the necessary boundary conditions for arbitrary geometries and arbitrary optical properties as desirable in case of tissue [42]. Alternative analytical approaches based on photon diffusion formalisms, random walk models, and maximum entropy principles have been explored for modeling polarized light transport in random medium such as tissues [42, 45, 46, 47, 48]. In these analytical/heuristic approaches, tissue is typically

modeled as a turbid medium having bulk-average scattering and absorption properties, where propagation leads to depolarization as a result of strong multiple scattering events (birefringence effects are often ignored). These approaches have derived simplified analytical relationships between various quantities of practical interests such as the degree of polarization (either linear or circular) of forward-scattered or back-scattered light from a turbid medium, average path lengths, the optical transport parameters of the medium, and so forth [45, 47, 48]. The main aim of these approximate analytical approaches has been to understanding the overall depolarization trends, its dependence on the scattering properties of the media, and on the incident state of polarization, and to design / optimize general polarization schemes to discriminate against multiply scattered photons for tissue imaging in 'simple' geometries. These approaches, while useful, are approximate by their very nature and typically neglect other simultaneously occurring complex tissue polarimetry events (such as linear birefringence, optical activity etc.). The applications of these models have thus been restricted to the 'tissue imaging' domain (employing polarization gating methods and various other co/cross polarization detection schemes). Interested readers are referred to references [42, 45, 46, 47, 48, 49] for the details of these models.

A more encompassing, accurate method is clearly needed for polarimetry applications involving quantitative assessment of tissue composition and micro-architecture. This can be accomplished by the polarization-sensitive Monte Carlo (PSMC) techniques. Monte Carlo (MC) technique is a general and robust approach for modeling light transport in random medium [43, 50], with its advantage of applicability to arbitrary geometries and arbitrary optical properties. In this statistical approach to radiative transfer, the multiple scattering trajectories of individual photons are determined using random numbers to predict the probability of each scattering event. It is also assumed that scattering events occur independently and exhibit no coherence effects. The superposition of many photon paths approaches the actual photon distribution in time and space. The initial Monte Carlo biophotonic models were developed for intensity calculations only and neglected polarization information [50], which has recently been incorporated in a number of implementations by keeping track of the Stokes vectors of propagating photon packets [49, 51, 52, 53, 54, 55]. A typical flow chart for PSMC model is shown in Fig. 13.3. Briefly in this model, position, propagation direction, and polarization of each photon are initialized and modified as the photon propagates through the medium. The photon's polarization, with respect to a set of arbitrary orthonormal axes defining its reference frame, is represented as a Stokes vector $\mathbf{S}$ and polarization effects are applied using medium Mueller matrices $\mathbf{M}$ [12]. The photon propagates in the sample between scattering events a distance sampled from the probability distribution $\exp(-\mu_t d)$, where the extinction coefficient $\mu_t$ is the sum of the absorption $\mu_a$ and scattering $\mu_s$ coefficients and $d$ is the distance traveled by the photon between scattering events [49, 50]. Upon encountering a scattering event, a scattering plane and angle are statistically sampled based on the polarization state of the photon and the Mueller matrix of the scatterer. The photon's reference frame is first expressed in the scattering plane and then transformed to the laboratory (experimentally observable) frame through multiplication of appropriate rotation matrices (reference frame manipulation) and by the Mueller matrix corresponding to the scattering event. Usually, the scattering Mueller matrix $\mathbf{M}$ is computed using Mie theory [4], which assumes the scattering medium to be comprised of discrete spherical scatterers. In principle, incorporation of scattering Mueller matrices for other non-spherical scatterers or the scattering matrices for other continuously fluctuating medium is also possible [49, 51]. Nevertheless, the evolution of polarization state of each photon packet is tracked (via the Stokes vectors) following successive scattering events. The absorption effects are incorporated after successive scattering events by reducing the photon weight by a factor $W = \frac{\mu_a}{\mu_a+\mu_s}$, as conventionally done in intensity-based MC models also [43, 50]. Upon encountering an interface (either an internal one, representing tissue layers of different optical properties, or an external one, representing external boundary), the probability of either reflection or transmission is calculated using Fresnel coefficients. Assuming no interference effects, the final Stokes vectors for light exiting the sample in a particular direction are computed as the sum of all the appropriate sub-populations of photons. The sample Mueller matrix can then be calculated

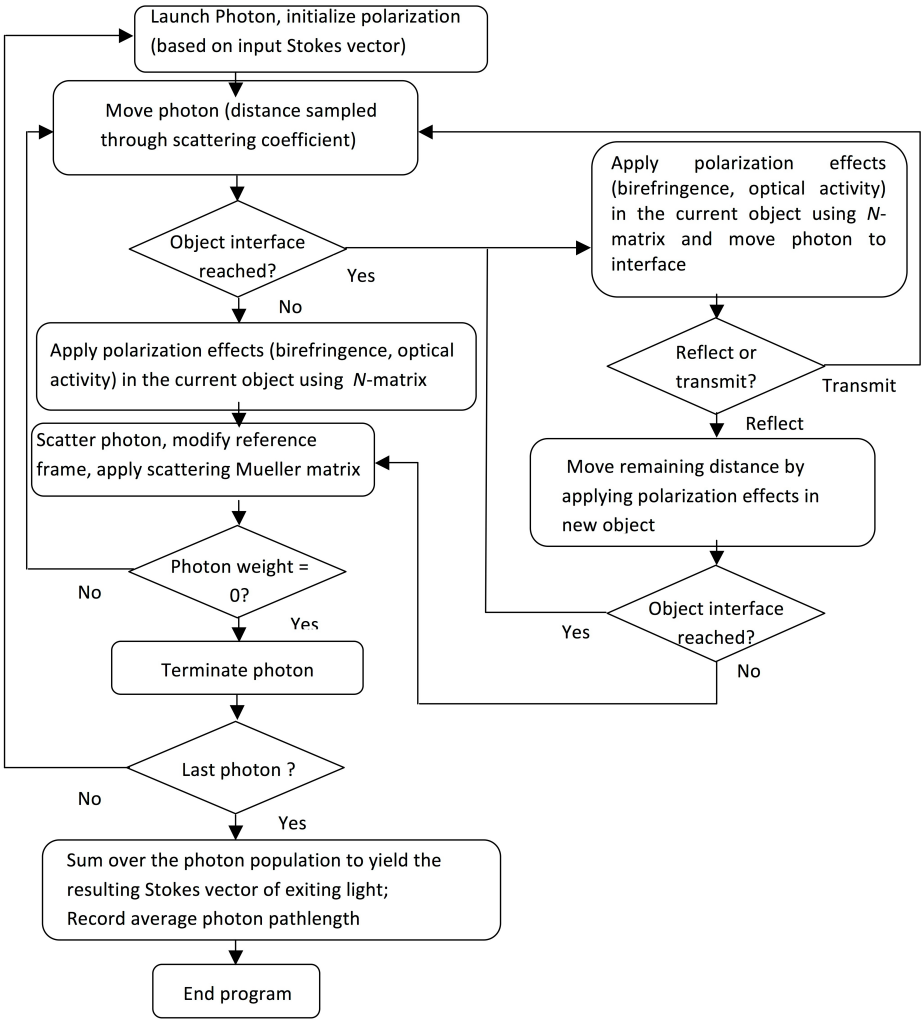


**Figure 13.3:** A flowchart representing the polarization-sensitive Monte Carlo model. (Adopted from [12].)

by sequentially changing the input polarization, recording the corresponding output Stokes vectors for each respective input states, and performing algebraic manipulations as described previously [52].

While the effects of scattering on the polarization evolution after successive scattering events can be modeled by the scattering Mueller matrix **M**, the effects of other medium polarimetry effects such as linear birefringence and optical activity can also be incorporated by including their corresponding Mueller matrices. However, this is not an obvious modeling step. Specifically, problems arise in modeling simultaneous polarization events in the presence of multiple scattering. Matrix multiplication of the Mueller matrices for individual polarization effects is not commutative ($\mathbf{M_A}\,\mathbf{M_B} \neq \mathbf{M_B}\mathbf{M_A}$), thus, different orders in which these effects are applied will have different effects on the output polarization. Yet in biological tissue, effects such as optical activity due to chiral molecules (e.g., glucose and proteins) and linear birefringence due to anisotropic tissue structures (e.g., collagen, elastin, and muscle fibers), must be incorporated into the model in the presence of

scattering. This problem is tackled through the use of so-called N-matrix formalism, which combines the effects into a single matrix describing them simultaneously [1, 56]. In this formalism, the matrix of the sample is represented as an exponential function of a sum of matrices (N-matrices), where each matrix in the sum corresponds to a single optical polarization effect [52, 56]. The issue of ordering is thus taken care, as matrix addition is always commutative. The N-matrices are the differential matrices representing the optical effect over an infinitely small optical pathlength, wherein several polarization effects can be written in a single matrix form. Conventionally, these N-matrices are $2 \times 2$ Jones matrices applicable to non-depolarizing media. For example, the N-matrix representing combined linear birefringence and optical activity is written as [1, 56]

$$N_{OA+LB} = \frac{1}{2}\begin{bmatrix} ig_0 & \chi \\ -\chi & -ig_0 \end{bmatrix} \tag{13.33}$$

Here, $g_0 = \frac{2\pi}{\lambda}\Delta n$ is the phase retardation per unit distance and $\chi$ is the optical rotation per unit distance. From this N-matrix, the parent non-differential M matrix is derived for the combined effect [52, 56]. The resulting Jones M-matrix is then converted to a Mueller matrix. Note that such a conversion from Jones to Mueller matrix is possible only for non-depolarizing matrices. This is indeed applicable to the PSMC model, since these matrices are incorporated between the scattering events, where no depolarization takes place. The resulting Mueller matrices for combined effects are thus applied to the photons as they propagate between scattering events. This approach enabled the combination of any number of simultaneously occurring polarizing effects. Finally, as shown in Fig. 13.3, the scattering histories of a large number of photon packets (typically $10^7$–$10^9$ photons are required to generate statistically acceptable results) are tracked as they propagate through the medium and are summed to yield the macroscopic parameters of practical interest (Stokes vectors, Mueller matrices, pathlength distributions, polarization statistics from different scattering histories, etc.).

In the simulation, circular and linear birefringence (these are the two most tissue polarimetry effects in addition to depolarization) are modeled through the optical activity $\chi$ in degrees per centimeter, and through the anisotropy in refractive indices ($\Delta n$), respectively [52]. Here, $\Delta n = (n_e - n_o)$ is the difference in refractive index along the extraordinary axis ($n_e$) and the ordinary axis ($n_o$). For simplicity, it is generally assumed that the direction of the extraordinary axis and the value for $\Delta n$ is constant throughout the scattering medium. (although recent research efforts are exploring the effects of multiple uniaxial domains of varying magnitude and orientation of birefringence). In each simulation, $n_e$ and $n_o$ are taken as input parameters and a specific direction of the extraordinary axis is chosen. As photons propagate between scattering events, the difference in refractive indices seen by the photons depends on the propagation direction with respect to the extraordinary axis. The effect is usually modeled using standard formulae describing the angular variation of refractive index in uni-axial medium [49, 52]. Similar to conventional MC model, the scattering and absorption properties are modeled using the optical transport parameters, scattering coefficient ($\mu_s$) and absorption coefficient ($\mu_a$).

The validity of the above PSMC model has been tested on experimental tissue simulating phantoms exhibiting simultaneous scattering and polarization properties, which are known and user-controlled *a priori* [12, 13, 29, 52]. These solid optical phantoms were developed using polyacrylamide as a base medium, with sucrose-induced optical activity, polystyrene microspheres-induced scattering and mechanical stretching to cause linear birefringence [52]. These phantom systems mimic the complexity of biological tissues, in that it exhibits simultaneous effects of linear birefringence, optical activity and depolarization due to multiple scattering. The experimental results of Mueller matrix measurements from these tissue phantoms and corresponding MC simulation results of analogous turbid media are presented and discussed subsequently.

## 13.5 Interpretation and Decomposition of Mueller Matrices

Polarimetric quantities, such as depolarization, optical activity, and linear birefringence can potentially serve as valuable metrics in biomedical applications. For example, changes in tissue mechanical anisotropy (resulting from disease progression or treatment response) can be probed with birefringence measurements [12, 57], and blood sugar levels can potentially be determined by measuring the optical rotation induced by the chiral glucose molecules [13, 14]. Despite the wealth of important properties which can be determined via tissue polarimetry, numerous complexities inhibit their straightforward extraction and interpretation.

Multiple scattering, a common phenomenon in biomedical polarimetry, not only causes extensive depolarization, but alters the state of the remaining polarized signal in a complex manner, for example, by scattering-induced diattenuation and by scattering-induced changes in the orientation of the polarization vector [21, 58]. Not only are polarimetric quantities difficult to measure reliably, but their co-occurrence in biomedical samples greatly complicates their unique interpretation. This problem manifests itself most clearly in trying to interpret the Mueller matrices of such samples: while the materials' transfer functions may qualitatively resemble those of one (or many) of the fundamental characteristics discussed in Section 13.2.3, their measured Mueller matrices generally look nothing like that of the idealized versions. Instead, they contain a convolved mix of otherwise individually recognizable properties, with much 'inter-element cross talk' obscuring potentially interesting polarization biometrics and hindering their interpretation. Thus, methods accounting for multiple scattering-induced effects, and capable of decoupling the individual contributions of simultaneously occurring basic polarimetric characteristics are required.

### 13.5.1 Decomposition into basic polarimetric components

Previous attempts at tissue polarimetry analysis have mostly utilized semi-empirical approaches by selectively measuring particular Stokes vectors or Mueller matrix elements of interest, based on the purported polarimetric signatures associated with various tissue anatomical or compositional characteristics [59]. However, recent studies have employed more general models to extract, quantify and interpret intrinsic tissue polarimetry characteristics by decomposing their measured Mueller matrices into more easily interpretable "basis" matrices [29, 30].

One particularly noteworthy method of Mueller matrix decomposition is known as the product, or Lu-Chipman, decomposition, after its inventors, who first demonstrated its validity in optically clear media [10]. This method consists of representing a sample Mueller matrix $\mathbf{M}$ as a product of three basis matrices

$$\mathbf{M} = \mathbf{M}_\Delta \mathbf{M}_R \mathbf{M}_D, \tag{13.34}$$

where the depolarizer matrix $\mathbf{M}_\Delta$ encodes the depolarizing effects of the medium, the retarder matrix $\mathbf{M}_\mathrm{R}$ describes its linear birefringence and optical activity, and the diattenuator matrix $\mathbf{M}_\mathrm{D}$ accounts for the effects of linear and circular diattenuation.

The diattenuation matrix $\mathbf{M}_\mathrm{D}$ is defined as

$$\mathbf{M}_D = \begin{bmatrix} 1 & \vec{d}^T \\ \vec{d} & \mathbf{m_D} \end{bmatrix}, \tag{13.35}$$

where $\mathbf{m}_D$ is the $3 \times 3$ matrix usually expressed as

$$\mathbf{m}_D = \sqrt{1-d^2}\,\mathbf{I} + \left(1 - \sqrt{1-d^2}\right)\hat{d}\hat{d}^T \tag{13.36}$$

Here $\mathbf{I}$ is the $3 \times 3$ identity matrix, and $\vec{d}$ is the diattenuation vector defined as

$$\vec{d} = \frac{1}{m_{1,1}} \begin{bmatrix} m_{1,2} & m_{1,3} & m_{1,4} \end{bmatrix}^T, \tag{13.37}$$

where $\hat{d}$ is its corresponding unit vector, determined by dividing the diattenuation vector by its magnitude $d$, given by

$$d = \frac{1}{m_{1,1}} \sqrt{m_{1,2}^2 + m_{1,3}^2 + m_{1,4}^2} \tag{13.38}$$

(The scalar $m_{ij}$ is the element of the sample Mueller matrix in the $i$-th row and the $j$-th column.) The elements $m_{1,2}$ and $m_{1,3}$ represent the linear diattenuation for horizontal/vertical and $\pm 45^\circ$ linear polarization respectively, and $m_{1,4}$ represents the circular diattenuation.

The product of the two remaining matrices in the decomposition can be expressed by right-multiplying the sample Mueller matrix by the inverse of $\mathbf{M}_D$, which motivates the following definition:

$$\mathbf{M}' = \mathbf{M}_\Delta \mathbf{M}_R = \mathbf{M}\mathbf{M}_D^{-1}. \tag{13.39}$$

The matrices $\mathbf{M}_\Delta$, $\mathbf{M}_\mathrm{R}$ and $\mathbf{M}'$ take the following form:

$$\mathbf{M}_\Delta = \begin{bmatrix} 1 & \vec{0}^T \\ P_\Delta & \mathbf{m}_\Delta \end{bmatrix}; \ \mathbf{M}_\mathrm{R} = \begin{bmatrix} 1 & \vec{0}^T \\ \vec{0} & \mathbf{m}_\mathrm{R} \end{bmatrix}; \ \text{and } \mathbf{M}' = \begin{bmatrix} 1 & \vec{0}^T \\ P_\Delta & \mathbf{m}' \end{bmatrix}, \tag{13.40}$$

where $P_\Delta = \frac{\vec{P} - m\vec{d}}{1-d^2}$, and the polarizance vector $\vec{P}$ is given by

$$\vec{P} = \frac{1}{m_{1,1}} \begin{bmatrix} m_{2,1} & m_{3,1} & m_{4,1} \end{bmatrix}^T \tag{13.41}$$

The blocks in Eq. (13.40) are naturally related as $\mathbf{m}' = \mathbf{m}_\Delta \mathbf{m}_R$. The matrix $\mathbf{m}_\Delta$ can be formed using the eigenvalues of $\mathbf{m}'\mathbf{m}'^T$ [10]; then, $\mathbf{M}_\Delta$ can be constructed and used to extract the net depolarization coefficient $\Delta$, another potentially useful biometric, using Eq. (13.11).

The remaining matrix $\mathbf{M}_\mathrm{R}$, which encodes the retardance, can be computed from Eq. (13.39), and the scalar value of the total retardance $R$ (representing the combined effect of linear and circular birefringence) is calculated as

$$R = \arccos\left(\frac{\mathrm{Tr}(\mathbf{M}_\mathrm{R})}{2} - 1\right) \tag{13.42}$$

The matrix $\mathbf{M}_\mathrm{R}$ can be further analyzed to extract the corresponding linear retardance $\delta$, as well as the optical rotation $\psi$, by separating it into the standard Mueller matrices corresponding to said parameters (Eqs. (13.14) and (13.15)). The values of these numbers can then be expressed directly in terms of the elements of $\mathbf{M}_\mathrm{R}$ as [29]

$$\delta = \arccos\left(\sqrt{(m_{\mathrm{R}2,2} + m_{\mathrm{R}3,3})^2 + (m_{\mathrm{R}3,2} - m_{\mathrm{R}2,3})^2} - 1\right) \tag{13.43}$$

and

$$\psi = \arctan\left(\frac{m_{\mathrm{R}3,2} - m_{\mathrm{R}2,3}}{m_{\mathrm{R}2,2} + m_{\mathrm{R}3,3}}\right). \tag{13.44}$$

In summary, the above decomposition (Eqs. (13.34)–(13.44)) operates on a sample Mueller matrix, and extracts several medium-specific polarimetry metrics of promising biomedical value, namely diattenuation ($d$), linear, circular and total depolarization ($\Delta$), linear retardance and its orientation ($\delta$ and $\theta$), and optical rotation ($\psi$).

Due to the non-commutative nature of matrix multiplication (i.e., $\mathbf{AB} \neq \mathbf{BA}$ in general), the order of the basis matrices in Eq. (13.34) is only one of six possible (distinct) permutations. The

arrangements are classified into two families: those where the diattenuator matrix is placed before the depolarizer (this includes Eq. (13.34)), and those where it is placed after [60]. The two groups are shown below:

$$\Delta D\ Family = \begin{cases} \mathbf{M}_\Delta \mathbf{M}_R \mathbf{M}_D \\ \mathbf{M}_\Delta \mathbf{M}_D \mathbf{M}_R \\ \mathbf{M}_\mathrm{R} \mathbf{M}_\Delta \mathbf{M}_D \end{cases} \quad D\Delta\ Family = \begin{cases} \mathbf{M}_\mathrm{D} \mathbf{M}_R \mathbf{M}_\Delta \\ \mathbf{M}_\mathrm{R} \mathbf{M}_D \mathbf{M}_\Delta \\ \mathbf{M}_\mathrm{D} \mathbf{M}_\Delta \mathbf{M}_R \end{cases} \tag{13.45}$$

It has been shown that of the six possible multiplicative orders, the Lu-Chipman decomposition and its reversal ($\mathbf{M}_\mathrm{D}\mathbf{M}_R\mathbf{M}_\Delta$), known as the reverse decomposition, always produce physically realizable Mueller matrices [60]. The other four decompositions can be obtained from the aforementioned two by employing similarity transformations. It has been found that in tissue polarimetry (in the absence of large $d$-values), the Lu-Chipman and reverse decompositions yield the correct description of the medium in question, based on the metrics presented above. The only differences between the forward and reverse orders were occasional sign changes in the derived values, indicating that both approaches extract the magnitudes of the polarization metrics in a self-consistent manner.

In an effort to eliminate any remaining ambiguity associated with the multiplicative order of the basis matrices, a more general kind of decomposition, known as the symmetric decomposition, has been developed, which factors an arbitrary depolarizing Mueller matrix into 5 matrices: a diagonal depolarizer $\mathbf{M}_\Delta$ multiplied to either side by an equivalent optical sequence containing diattenuators and retarders [61]. This decomposition can be expressed as

$$\mathbf{M} = \mathbf{M}_{\mathrm{D}2}\mathbf{M}_{\mathrm{R}2}\mathbf{M}_\Delta\mathbf{M}_{\mathrm{R}1}^T\mathbf{M}_{\mathrm{D}1} \tag{13.46}$$

As is apparent from the six different decompositions given in Eq. (13.45), the ambiguity in the derived polarization parameter mainly arises depending upon whether the diattenuator matrix is placed before or after the depolarizer. The symmetric decomposition helps in interpretation and analysis of any experimental Mueller matrix in that it does not impose any restriction on the preferred sequential occurrence of the diattenuation effect. Thus, it allows for extraction of the constituent polarization parameters of any complex system with less ambiguity. However, it should be mentioned, this approach also does not really address the issue of *simultaneously* occurring polarization effects, which is typically encountered in tissue. In order to address this issue, a more general kind of decomposition based on differential matrix formalism of the Mueller calculus, has recently been developed [62]. This formalism was originally proposed by Azzam for non-depolarizing optical media [63]; it has been extended and generalized to incorporate depolarization effects [62]. Within the differential matrix formalism, all elementary polarization and depolarization properties of the medium are contained in a single differential matrix representing them simultaneously. Thus, this approach is expected to be more suitable for Mueller matrix polarimetry analysis of tissues, exhibiting *simultaneous* polarization effects. An interested reader is referred to the literature [62, 63] for the details of the differential Mueller matrix formalism.

There exists another type of product decomposition, known as the Cloude decomposition, which expresses an arbitrary depolarizing Mueller matrix $\mathbf{M}$ as a *sum* of a non-depolarizing Mueller matrix $\mathbf{M}_{n\Delta}$(which can be further decomposed using the above-mentioned process) and an ideal polarizer $\mathbf{M}_\Delta$ [64]. While theoretically interesting and practically attractive (matrix addition is commutative, so there is no order ambiguity as in product-based decompositions), Cloude decomposition has not been used in tissue polarimetry.

The decompositions presented here hold great promise for their ability to extract useful biological metrics from the Mueller matrices of complex samples, but they require comprehensive validation; more specifically, the effects of various decomposition processes, permutations of basis matrices, the detection geometry and the propagation path of multiply scattered photons on the extracted metrics must be thoroughly examined, and above all, the derived parameters must be shown to accurately represent the true polarimetric properties of the medium in question. Several studies have

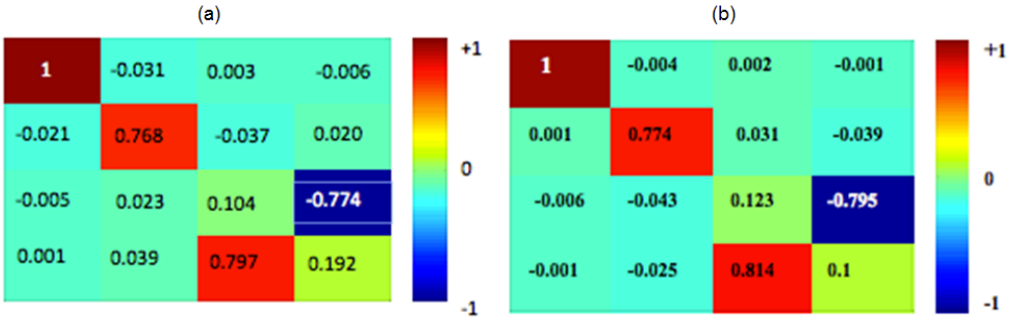


**Figure 13.4:** The Mueller matrices (a) experimentally recorded in the forward (transmission) detection geometry from birefringent (extension = 4 mm, corresponding to a value of linear retardance $\delta$ = 1.345 rad for a clear phantom), chiral concentration of sucrose = 1 M, $\chi = 1.96$ degree cm$^{-1}$ turbid ($\mu_s = 30$ cm$^{-1}$, $g = 0.95$) phantom of thickness of 1 cm; (b) generated through the PSMC model, using the same controlled input scattering and polarization parameters (linear birefringence $\Delta n = 1.36 \times 10^{-5}$, corresponding to $\delta = 1.345$ rad, $\chi = 1.96$ degree cm$^{-1}$, $\mu_s = 30$ cm$^{-1}$, $g = 0.95$) as that of the experimental phantom. *The excellent agreement between the experimental and the simulated Mueller matrices emphasizes the capability of the PSMC model in simulating complex tissue polarimetry effects, including simultaneous optical activity and birefringence in the presence of multiple scattering.* The results of the decomposition of the experimental Mueller matrix are presented in Table 13.1.

begun investigating these issues [12, 29, 65] and some of the results are presented in the following section.

### 13.5.2 Experimental verification of decomposition

Figure 13.4 provides an example of the Lu-Chipman decomposition applied to the experimentally derived Mueller matrix of a control sample, composed of a solid polyacrylamide, and exhibited simultaneous depolarization, linear birefringence and optical activity. Its Mueller matrix was measured using forward detection geometry. While the sample's measured matrix has a rather complex form, with all sixteen elements being non-zero, the resulting basis matrices exhibit simpler features; notably, a high level of symmetry and many zero off-diagonal elements. The scalar parameters ($\Delta$, $d$, $\delta$, and $\psi$) derived from this decomposition are presented in Table 13.1, showing excellent agreement with the controlled inputs.

The values for parameters $\delta$ and $\psi$ determined from the decomposition of Mueller matrices corresponding both to non-scattering (no-microspheres) and turbid ($\mu_s = 30$ cm$^{-1}$, $g = 0.95$) optically active ($\chi = 1.96$ °cm$^{-1}$) phantoms with increasing birefringence (sample extension of 0–4 mm, $\delta = 0$–1.34 rad), are displayed in Fig. 13.5 [29]. The values are in close agreement with the controlled experimental inputs ($\psi \approx 1.96°$ and $\delta = 1.34$ rad at 4 mm of extension), for both clear and scattering samples. This result suggests that the depolarizing effects of multiple scattering have been properly isolated and accounted for in the decomposition.

Figure 13.6 shows the derived linear retardance ($\delta$) and optical rotation ($\psi$) for Monte Carlo generated Mueller matrices, using chiral molecule concentration as the independent variable [30]. As in the experimental case, the values are in excellent agreement with the input parameters ($\delta =$ 1.4 rad and $\chi = 1.96°$ cm$^{-1}$ at 1 M sucrose) for both non-scattering and turbid media, showing self-consistency in inverse decomposition analysis and successful decoupling. The small increases in optical rotation observed in turbid media (in both the experimental phantoms or the corresponding

**TABLE 13.1:** The upper panel shows the experimentally determined Mueller matrix, and its decomposition into three basis matrices. The lower panel presents the polarization parameters extracted from these matrices in the second column, and the corresponding expected values in the third. The input control values for linear retardance $\delta$ and optical rotation $\psi$ were obtained from measurement on a clear ($\mu_s = 0$ cm$^{-1}$) phantom having the same extension (4 mm) and similar concentration of sucrose (1 M) as that of the turbid phantom, and corrected for the increased pathlength due to multiple scattering (determined from Monte Carlo modeling). The expected value for the net depolarization coefficient $\Delta$ was determined from the Monte Carlo simulation of the experiment. (Adopted from reference [29]).

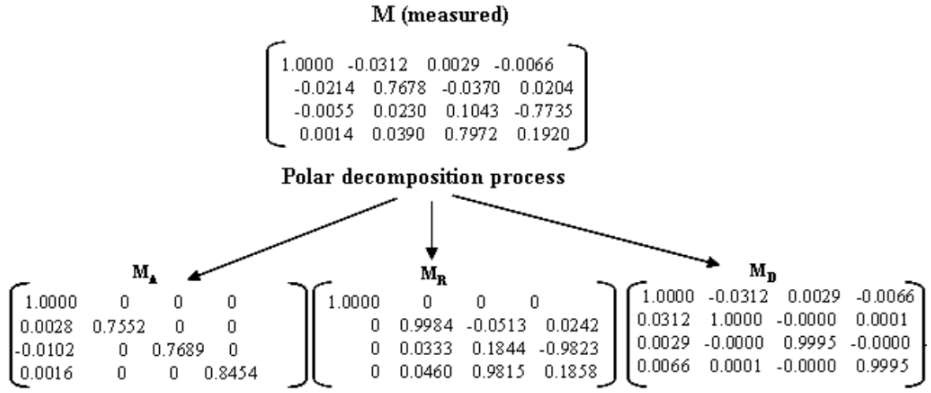


| Parameters | Derived parameters(from $\mathbf{M}_\Delta$, $\mathbf{M}_R$, $\mathbf{M}_D$) | Expected value |
|---|---|---|
| d | 0.032 | 0 |
| $\delta$ | 1.384 rad | 1.345 rad |
| $\psi$ | 2.04° | 2.07° |
| $\Delta$ | 0.21 | 0.19 |

Monte Carlo simulated scattering media) likely arise from the increased optical pathlength caused by multiple scattering, thus resulting in accumulations of $\psi$ values [29].

The illustrative results discussed above are based on Mueller matrices recorded in the forward detection geometry, but the extension of this approach to backward detection geometry (which is well-suited for *in-situ* measurements) is warranted, and has also been validated [65]. While the later geometry is important for conceptual and practical reasons, it offers additional technical hurdles; notably, the polarization parameters associated with the intrinsic polarimetric properties of the sample in question can be difficult to infer since they are more strongly coupled with scattering-induced effects. At detection positions sufficiently close to the exact backscattering direction, the contribution of the backscattered (singly or weakly scattered) photons can cause large apparent scattering-induced diattenuation and linear retardance effects, even from isotropic ($\Delta n = 0$) scattering samples. This additional contribution masks the intrinsic polarimetric parameters of interest and hinders their accurate determination. However, it has been shown that as one moves away from the exact backscattering geometry, the magnitude of scattering-induced diattenuation and retardance gradually diminish and eventually become weak (magnitudes $d \leq 0.05$, $\delta \leq 0.1$) for detection positions located at distances larger than a transport length away from the point of illumination ($r > l_{tr}$, where $l_{tr} = 1/\mu_s(1-g)$ is the transport scaling length). Thus one possible method to accurately measure polarization parameters from a turbid medium using backward detection geometry is to

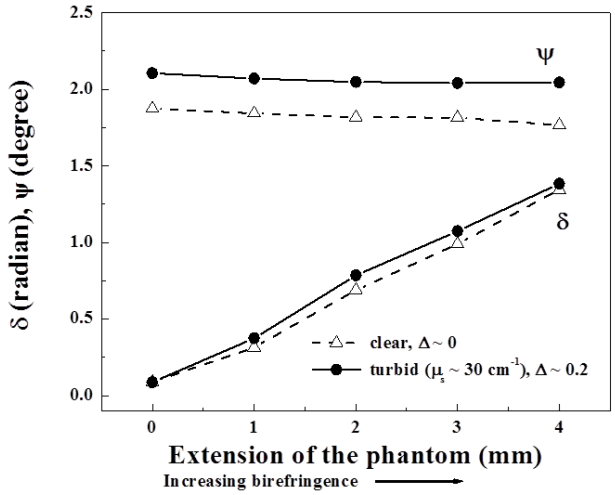


**Figure 13.5:** Linear retardance $\delta$ and optical rotation $\psi$ derived from the decomposition of experimentally determined Mueller matrices of solid chiral ($\chi$ = 1.96° cm$^{-1}$, corresponding to 1 M concentration of sucrose) phantoms with varying degrees of strain-induced birefringence (extension of 0–4 mm, $\delta$ = 0–1.345 radian). Results are shown from both clear ($\mu_s = 0$ cm$^{-1}$) and turbid ($\mu_s$ = 30 cm$^{-1}$, $g = 0.95$) phantoms, and the values for the decomposition-derived depolarization coefficient $\Delta$ are also noted. The measurements were performed in the forward detection geometry ($\gamma = 0°$) through a 1 cm×1 cm ×4 cm phantom. The symbols correspond to experimental data and the lines serve to guide the eye. (Adapted from references [12, 30].)

perform measurements at a distance larger than a transport length away from the point of illumination [65].

Ongoing examination of Mueller matrix decomposition for tissue-like complex turbid media (whose constituents properties are controlled and known *a priori*), with both experimental and Monte Carlo-simulated matrices, have shown that in turbid media with weak diattenuation (magnitude $d \leq 0.1$), the decomposition-inferred parameters are essentially independent of the multiplicative order of the basis matrices, and that they accurately reflect the known sample properties. This is an important result, as it suggests that the measurement and decomposition techniques discussed above may be directly applicable to tissues, in which biological molecules (such as nucleic acids, amino acids and proteins) exhibit weak dichroism or diattenuation, which would otherwise be masked by more pronounced polarimetric effects.

By extrapolating the results from Section 13.5.1, one might suspect that the parameters derived from actual tissue should be independent of multiplication order in the decomposition. This conjecture is verified in Table 13.2, which provides an example of a decomposition analysis performed on the Mueller matrix recorded from dermal tissue of an athymic nude mouse [66]. The basis matrices corresponding to Lu-Chipman and reverse decompositions are shown in this table, as well as the corresponding values of the extracted polarization parameters. (The other four permutations in Eq. (13.45) were ruled out in light of physical or mathematical considerations [60, 67].) The similarity between the elements of the basis matrices corresponding to both decompositions suggests that the polarimetric interactions of photons passing through tissue occur simultaneously, rather than in a preferred sequence, as expected. Most importantly, the excellent agreement between the parameters extracted from two decompositions and their true values underscores the validity of the

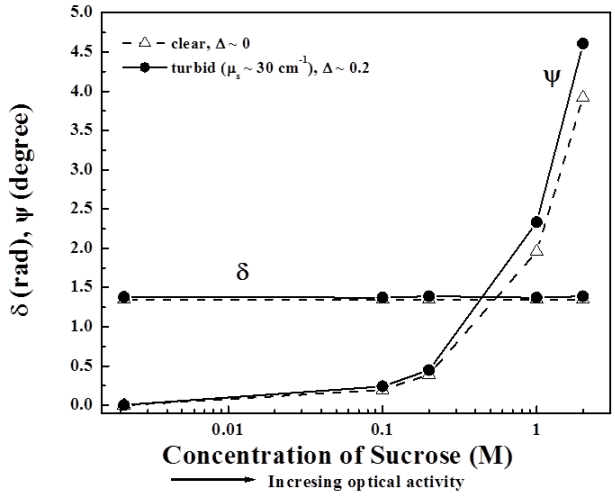


**Figure 13.6:** The values of $\delta$ and $\psi$ extracted from the decomposition of Monte Carlo-generated Mueller matrices from birefringent media (linear birefringence $\Delta n = 1.36 \times 10^{-5}$, corresponding to $\delta$ = 1.345 rad for a path length of 1 cm, the axis of linear birefringence was kept along the vertical direction, orientation angle = 90°) with varying levels of chirality ($\chi$ = 0, 0.196, 0.392, 1.96, and 3.92° cm$^{-1}$, corresponding to concentration of sucrose of 0, 0.1, 0.2, 1, and 2 M, respectively). Results are presented for both clear ($\mu_s$ = 0 cm$^{-1}$) and turbid ($\mu_s$ = 30 cm$^{-1}$, $g = 0.95$) media. The symbols represent data points and the lines serve to guide the eye. (Adapted from references [12, 30].)

decomposition formalism and its self-consistency with respect to the ambiguity of ordering.

Decoupling and quantification of the individual intrinsic tissue polarimetry characteristics is thus enabled by the polar decomposition analysis, despite their simultaneous occurrence, even in the presence of the numerous complexities due to multiple scattering. The ability to isolate individual polarization properties provides a potentially valuable non-invasive tool for biological tissue examinations. The following section examines the ongoing and prospective biomedical applications of the intrinsic tissue polarimetry characteristics.

## 13.6 Biomedical Applications of Polarimetric Measurements

A widely-pursued application of polarized light methods is for tissue imaging, which we only mention in passing (with sufficient citations to refer an interested reader). These imaging approaches encompass polarization-gating and various parallel/cross linear polarization arrangements for enhancing skin examinations in dermatology and tumour margins imaging, specifically intra-operatively / following surgical resections. An interested reader is referred to a recent review on polarized light imaging of biological tissues by Jacques [68]. Another imaging-related biomedical application of polarimetry is its use in microscopy, especially nonlinear microscopy. Again, the reader is referred to an excellent and comprehensive review of recent developments in this exciting field [69]. Outside the tissue imaging domain, quantitative assessment of tissue composition

**TABLE 13.2:** The upper panel shows an experimentally determined Mueller matrix measured from dermal tissue of an athymic nude mouse, and its decomposition into three basis matrices. The original matrix was measured *in vivo* from a dorsal skinfold window chamber mouse model, using a high sensitivity turbid-polarimetry system. The basis matrices in the uppermost decomposition were obtained using the order $\mathbf{M} = \mathbf{M}_\Delta \mathbf{M}_R \mathbf{M}_D$, whereas those in the lower set correspond to the order $\mathbf{M} = \mathbf{M}_D \mathbf{M}_R \mathbf{M}_\Delta$. The lower panel shows the derived polarimetric parameters corresponding to each decomposition. Note that this is the first demonstration of Mueller matrix decomposition in live tissues [66].

**M (measured)**

$$\begin{pmatrix} 1 & 0.0707 & 0.0348 & -0.0060 \\ 0.0480 & 0.4099 & 0.0077 & 0.0650 \\ 0.0162 & -0.0184 & 0.2243 & -0.3580 \\ 0.0021 & -0.0465 & 0.3571 & 0.1783 \end{pmatrix}$$

$\mathbf{M}_\Delta$

$$\begin{pmatrix} 1 & 0 & 0 & 0 \\ 0.0193 & 0.4006 & 0 & 0 \\ 0.0076 & 0 & 0.4596 & 0 \\ -0.0060 & 0 & 0 & 0.3768 \end{pmatrix}$$

$\mathbf{M}_R$

$$\begin{pmatrix} 1 & 0 & 0 & 0 \\ 0 & 0.9935 & 0.0697 & 0.0897 \\ 0 & 0.0435 & 0.4960 & -0.8673 \\ 0 & -0.1049 & 0.8655 & 0.4897 \end{pmatrix}$$

$\mathbf{M}_D$

$$\begin{pmatrix} 1 & 0.0707 & 0.0348 & -0.0060 \\ 0.0707 & 0.9994 & 0.0012 & 0 \\ 0.0348 & 0.0012 & 0.9975 & 0 \\ -0.0060 & 0 & 0 & 0.9969 \end{pmatrix}$$

$$\begin{pmatrix} 1 & 0.0516 & 0.0301 & -0.0037 \\ 0 & 0.3994 & 0 & 0 \\ 0 & 0 & 0.4588 & 0 \\ 0 & 0 & 0 & 0.3758 \end{pmatrix}$$

$$\begin{pmatrix} 1 & 0 & 0 & 0 \\ 0 & 0.9935 & 0.0701 & 0.0898 \\ 0 & 0.0436 & 0.4960 & -0.8672 \\ 0 & -0.1047 & 0.8655 & 0.4898 \end{pmatrix}$$

$$\begin{pmatrix} 1 & 0.0480 & 0.0162 & 0.0021 \\ 0.0480 & 0.9999 & 0.0004 & 0 \\ 0.0162 & 0.0004 & 0.9988 & 0 \\ 0.0021 & 0 & 0 & 0.9987 \end{pmatrix}$$

| Parameters | Derived parameters using the order $\mathbf{M}_\Delta \mathbf{M}_R \mathbf{M}_D$ | Derived parameters using the order $\mathbf{M}_D \mathbf{M}_R \mathbf{M}_\Delta$ |
|---|---|---|
| d | 0.079 | 0.051 |
| $\delta$ | 1.06 rad | 1.058 rad |
| $\psi$ | 0.51° | 0.50° |
| $\Delta$ | 0.58 | 0.59 |

and micro-architecture are two particularly attractive and promising applications of polarized light methods in medicine, and these tissue characterization approaches will be reviewed below.

### 13.6.1 Quantitative glucose sensing with Stokes/Mueller polarimetry

Glucose is an optically active (chiral) molecule, and its structural asymmetry imposes a unique 'fingerprint' on polarized light that interacts with it. For example, the plane of polarization of linearly polarized light is rotated upon passage through a glucose solution, by an amount proportional to the light interaction length, its concentration, and its wavelength-dependent rotatory power (a known quantity). As such, the glucose concentration in clear media can be easily determined by polarimetric measurements of optical rotation (this is routinely done, for example in biochemical laboratories and in the food industry [1, 70]). Can a similar polarized light approach be used in biomedicine, for example to noninvasively determine blood glucose levels in diabetic patients? If yes, this would represent a tremendous advance, as noninvasive glucose sensing remains arguably one of the most pressing unsolved problem in clinical medicine. Numerous approaches have been, and are being actively explored to address this difficult challenge [14].

Unfortunately, the polarimetric approach for biomedical glucometry is also fraught with difficul-

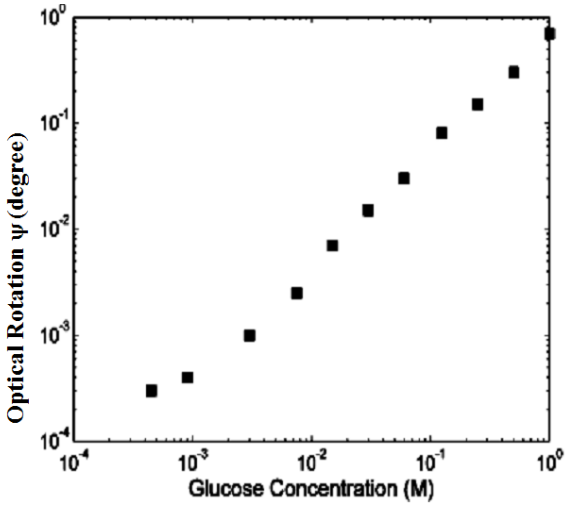


**Figure 13.7:** Logarithmic plot of experimentally determined optical rotation as a function of glucose concentration in scattering media (1.4 $\mu$m diameter polystyrene microspheres in water, $\mu_s \sim 28$ cm$^{-1}$) down to physiological glucose levels. Measurements were performed using forward detection geometry ($\gamma = 0^\circ$) through 1 cm of turbid media in a quartz cuvette. (Adopted from [13, 71].)

ties. Unlike its 'easy' transparent media counterpart, light propagating in tissue does not have a unique interaction length which is needed to convert measured optical rotation to glucose concentration; other dominant and complex tissue effects such as multiple scattering and inhomogeneous birefringence depolarize the light and alter its polarization properties (including causing chirality-unrelated apparent rotation of its linear polarized fraction), the glucose chirality effects are rather weak (owing to the low physiologic levels of blood glucose, in the range of 3–30 mM, or ~0.5–5 gm/L of blood, yielding optical rotations in the milli-degree range), and other chiral molecules present in tissue mask the already-weak glucose signal. Nevertheless, we and others have performed careful fundamental feasibility studies towards polarimetric tissue glucometry, as briefly summarized below.

Figure 13.7 shows milli-degree-level optical rotations $\psi$ induced by physiological (millimolar) glucose concentrations in a 1-cm-thick polystyrene microsphere scattering phantom ($\mu_s \sim 30\,\text{cm}^{-1}$) [71]. This study was performed with a sensitive polarimetric system that utilized polarization modulation and synchronous detection with a dual balanced photodetector approach, optimized to measure weak polarization signals in largely depolarized background. The results shown are for the forward-direction transmission geometry, with the rotations calculated from the determined Stokes vectors via $\psi = 0.5\tan^{-1}(u/q)$. The forward transmission direction was selected to enable direct results interpretation (pathlength $\geq$ cuvette thickness, rotation directly proportional to glucose concentration) and to minimize rotation artefacts unrelated to chirality. The drawback of transmission geometry is severe depolarization, limiting polarimetric measurements to 2–3 mm thicknesses of tissue [18, 21, 66]; this is why the scattering coefficient for this study in 1-cm-thick cuvette was lowered to $\sim$ 30% of typical tissue levels. Nevertheless, this preliminary study shows the polarimetric potential for measuring physiological glucose levels in tissue-like scattering media.

Backwards detection geometry in reflection mode is more convenient for practical tissue applications, yet the chirality-unrelated optical rotation artefacts can be severe [55]. A method to suppress these artefacts is thus essential, and the Mueller matrix polar decomposition methodology can be used to advantage here. Figure 13.8 shows the variations in the scattering induced apparent rota-

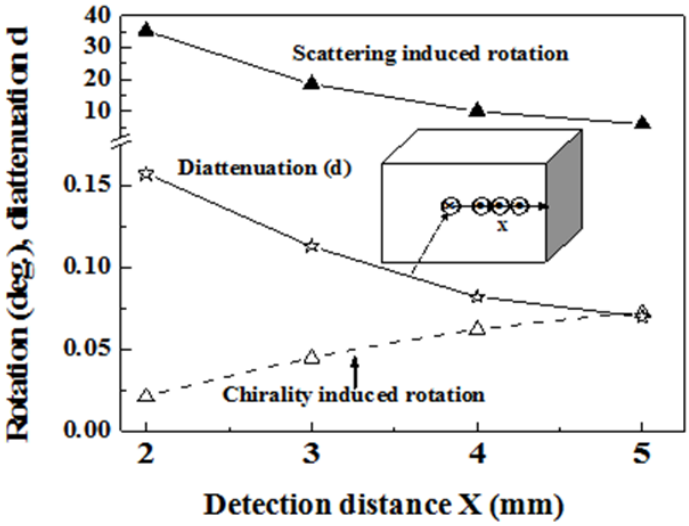


**Figure 13.8:** Optical rotation ($\psi$), derived from the decomposition of Monte Carlo generated Mueller matrices (open triangles), of backscattered light as a function of distance from the centre of the incident beam of a chiral ($\chi = 0.082$ degree cm$^{-1}$, corresponding to 100 mM concentration of glucose) isotropic turbid medium ($\mu_s = 30$ cm$^{-1}$, $g = 0.95$, thickness $t = 1$ cm). The solid triangles represent the corresponding scattering induced rotation of the polarization vector, derived from the Stokes parameters of the scattered light (for incident polarization state $S = [1,0,1,0]^T$ ). The inset shows the backwards detection geometry. *Decomposition analysis revealed that the large scattering-induced (chirality-unrelated) apparent rotation is due to linear diattenuation (shown by open asterisk), and can be decoupled from the chirality-induced rotation.* The chirality-induced rotation approaches zero as the detection angle approaches the exact backscattering detection ($\chi =$ 0 degree cm$^{-1}$, data not shown). The symbols represent PSMC-generated points and the lines serve to guide the eye. (Adopted from [30, 75].)

tion and in the chirality-induced true optical rotation as a function of offset distance from the point of illumination, in the backscattering direction [12, 30]. As seen, the scattering rotation artefact can be nearly an order of magnitude larger than the small chirality effect, completely dominating and masking the presence of glucose. Yet polar decomposition can effectively separate out these two differently sized contributions, revealing the glucose signal in this important yet artefact-prone detection geometry. Despite the highly preliminary nature of this study – the complicating effects of other chiral confounders, experimental validation of these Monte Carlo simulations results, signal changes due to varying optical absorption, and other complexities yet to be evaluated – this does suggest a method to tease out small glucose specific signals in highly scattering tissues. In combination with Monte Carlo-determined pathlength distributions, we are currently investigating spectroscopic polarimetry coupled with chemometric regression analysis to isolate glucose rotations from contributions of other chiral confounders [72]. Further, given the extremely challenging nature of the noninvasive glucometry problem, it is worthwhile to consider hybrid approaches; that is, combining spectral turbid polarimetry with another diagnostic modality (e.g., photoacoustics) by carefully drawing on each technique's complimentary strengths in isolating small tissue glucose levels.

### 13.6.2 Mueller matrix quantification of structural anisotropy in tissue

Tissue structural asymmetries can stem from aligned orientations of tissue fibrilar components, such as connective tissues composed of collagen, elastin or cartilage, and from elongated asymmetric cells such as smooth muscle or neurons. These structural alignments often result in tissue birefringence, which can be probed with polarized light. Since the structural and functional properties of these tissues change with disease initiation and progression or in response to therapies, birefringence measurements may represent a sensitive metric for assessing tissue status. The polar decomposition platform is the preferred methodology in this context for two reasons: (1) it is essential to separate out the birefringence signature from other complex and simultaneously-occurring compounding effects, and (2) other tissue metrics that are derived 'for free' using this methodology (e.g., diattenuation, depolarization, and potentially other metrics not discussed above, such as retardance ellipticity [10, 73]) may offer additional complimentary biophysical information that can help generate a more complete picture of the complex nature of the interrogated biological tissue. Below we present a cardiologic and a urological study to demonstrate the utility of polarimetric monitoring of tissue anisotropy.

#### 13.6.2.1 Cardiologic studies in the heart

Myocardial muscle is highly structured and anisotropic, due in part to the aligned arrangement of cardiomyocytes and collagen fibers. It thus exhibits high levels of linear birefringence in its natural healthy state. Following a heart attack, there is significant structural remodelling, with cardiomyocyte atrophy and an increase in fibrotic collagen content (scar tissue), often arranged in chaotic and random fashion. One thus expects a lowering of structural anisotropy, manifest as a decrease in polarimetrically-derived linear birefringence levels. Further, various post-infarct therapies (e.g., stem cell tissue regeneration) aim to restore heart muscle towards its normal structure, and more importantly restore some of its functional status [74]. It is thus interesting to apply the polarimetric polar-decomposition methodology to quantify cardiac linear birefringence, and test its utility to monitor the severity of heart infarct and to gauge the success of subsequent regenerative treatments.

Figure 13.9 summarizes the pertinent results from such a study, performed in transmission through 1-mm thick *ex-vivo* slabs of Lewis rat hearts after myocardial infarction, both with and without stem cell treatments [30]. Point polarimetry measurements (obtained with PEM-based polarization modulation and synchronous detection system) and imaging results (with static polarization components and a camera system) are shown, with both sets analyzed via the Mueller matrix polar decomposition approach. The reader is referred to the original literature for the many details of biological model and measurement specifics [30, 75]. Several interesting trends are evident from Fig. 13.9. These include the high levels of native linear birefringence, a dramatic decrease in the affected areas following the infarct, and partial recovery of these up towards pre-infarct birefringence levels following stem cell regenerative treatments. This birefringence increase suggests myocardial microstructural remodelling caused by therapeutic stem cell injection, and was subsequently confirmed by histology [75, 76]. Monitoring the micro-organizational state of cardiac tissue via tissue polarimetry thus appears possible, with the important added advantage (not feasible with many other techniques) of being able to assess and quantify regenerative treatments of infarcted myocardium.

Additional metrics that emerge from the polar decomposition analysis essentially for 'free', for example diattenuation and depolarization (and circular birefringence/optical rotation, if any), contain useful biological microstructural and compositional information that can supplement the linear birefringence results [66]. We are currently examining optimal means of combining these various polarimetric tissue characterization metrics; suffice it to say for now that the measurement and quantification of tissue linear birefringence offers a promising means of assessing the health, and pathology, of aligned biological tissues such as found in the heart. Similar trends are emerging in oncology, with several recent reports detailing polarimetric contrast between normal and cancerous tissues in the oral and cervical cavities [77, 78], with potential application for early diag-

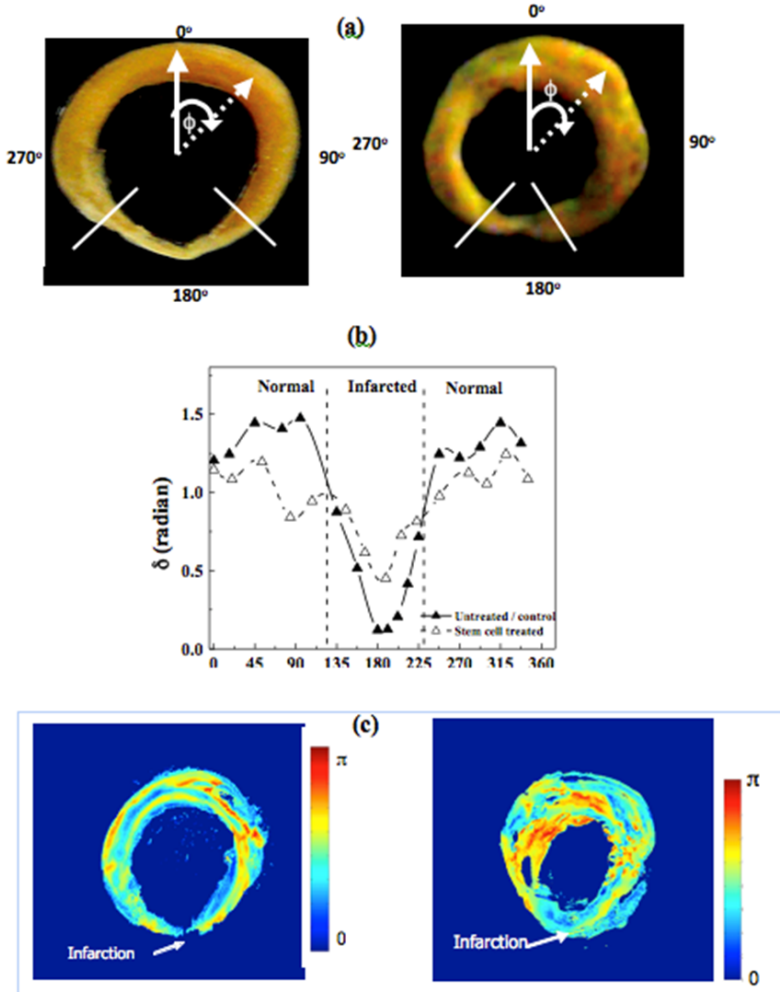


**Figure 13.9:** Linear retardance $\delta$ extracted from experimentally determined Mueller matrices corresponding to 1 mm-thick tissue sections from Lewis rat hearts following myocardial infarction. (a) White-light photographs of untreated (left panel) and stem cell treated (right panel) tissue. (b) Mueller matrix-derived linear retardance ($\delta$) values at different angular positions from the untreated (solid triangles) and treated (open triangles) samples. (c) The corresponding linear retardance ($\delta$) images for the same tissue, derived from imaging polarimetry measurements. (Adopted from [30, 72].)

nosis/detection and for intraoperative surgical margins assessment [79]. However, many technical and conceptual challenges in quantifying biological anisotropy via the linear birefringence approach remain; for example, additional studies dealing with nonlinear microscopy validation, unique determination of true birefringence magnitude and orientation, comparisons with diffusion-tensor MR, and effects of spatially heterogeneous birefringence, have recently been undertaken [80, 81, 82].

#### 13.6.2.2 Urologic studies in the bladder

Bladder is another internal organ whose structure and function engenders anisotropic tissue structure. Its purpose is to store and then expel urine, and its wall layers extend and then contract to

allow this to happen. Microstructural remodelling in its epithelial layers is known to occur under mechanical distension and during various disease processes (e.g., bladder outlet obstruction) [83, 84, 85, 86, 87]. As a step towards developing a turbid polarimetry platform for human bladder pathology studies, we have recently obtained birefringence maps in normal *ex-vivo* distended rat bladders that demonstrate the differential response of different bladder regions (dome, ventral and dorsal locations) to changes in filling pressure [88]. The results of Fig. 13.10 were obtained under pressures that represent typical physiological ranges in normal rodent (and human) bladders; as we progress to examine pathological cases, the upper end of the pressure range will likely have to increase. As seen, the dome region of the bladder shows maximum birefringence when the bladder is distended to high pressures, whereas the ventral tissues remains roughly isotropic during distension. In addition, the average anisotropy direction is longitudinal, along the urethra to dome. Using the analysis in Section 13.2.3.3, we converted the retardance values (derived from polar decomposition) to birefringence by measuring the bladder wall thickness with OCT, and by estimating the average photon pathlength in this reflection geometry via our polarization-sensitive Monte Carlo model (Section 13.4). The derived wall anisotropy trends thus represent an intrinsic tissue property of its anisotropy/organization independent of thickness, to better aid in understanding the structure-functions relation in healthy bladders. These new insights into the wall microstructure anisotropy of *ex vivo* distending bladders may also help improve the functionality of the artificially engineered bladder tissues [89, 90].

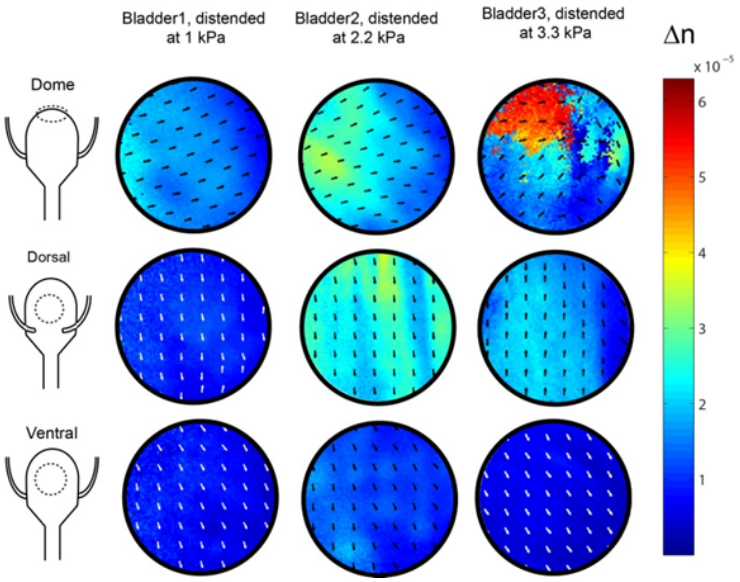


**Figure 13.10:** Regional anisotropy (birefreingence) images of healthy *ex-vivo* intact rat bladders distended to 1.0, 2.2, and 3.3 kPa. The polarization measurements were performed in reflection geometry (25° off the exact backscattering direction). Retardance maps were derived by polar decomposition analysis, and converted to birefringence using OCT-measured bladder wall thickness and Monte Carlo-derived average pathlength. The rows show the birefreingence images from the anatomical region indicated by the dotted contour on the *ex-vivo* bladder cartoon in the left column. The color represents the value of $\Delta n$ (color bar on right), and the arrows indicate the anisotropy direction. The field of view is 2 mm in diameter. Note the maximum birefringence in the dome region upon maximum distension, and the overall longitudinal anisotropy orientation (along urethra-dome axis). (Adopted from [88].)

## 13.7 Conclusion

Biological tissues are not easily amenable to polarimetric investigation, owing to extensive polarization loss caused by multiple scattering and by spatially-varying birefringence. Nevertheless, it is possible in many circumstances to reliably detect some surviving polarization states after fully polarized (linear, circular, elliptical) light is shone on tissue. Several issues then emerge, including (1) how to reliably measure and characterize this surviving fraction, (2) how to interpret these measured polarization signals and relate them to tissue properties of interest, and (3) how to apply this emerging methodology to biomedical problems of interest. We have addressed various aspects of (1)–(3) in this chapter, concentrating on applications pertaining to polarimetric detection of optical activity (for glucose sensing) and birefringence imaging (for tissue anisotropy assessment). The general trend towards polarization quantification, exemplified by Mueller matrix decomposition, has been noted, as is essential for further advances in this challenging field. Coupled with improvements in experimental methods and theoretical models, recent resurgence of interest and research activity, and expanding range of exciting biomedical applications, the near- and long-term future of tissue polarimetry appears promising.

## Acknowledgements

NG would like to acknowledge IISER Kolkata, an autonomous research and teaching institute funded by the Ministry of Human Resource Development, Govt. of India, for support

## References


[1] D.S. Kliger, J.W. Lewis, and C.E. Randall, *Polarized Light in Optics and Spectroscopy*, Academic Press–Harcourt Brace Jovanovich, New York (1990).

[2] C. Brouseau, *Fundamentals of Polarized Light, a Statistical Optics Approach*, Wiley, New York (1998).

[3] E. Collett, *Polarized Light: Fundamentals and Applications*, Marcel Dekker Inc., New York (1990).

[4] C.F. Bohren and D.R. Huffman, *Absorption and Scattering of Light by Small Particles*, Wiley, New York (1983).

[5] V. Ronchi, *The Nature of Light*, Harvard University Press, Cambridge, Massachusetts (1970).

[6] E. Hecht, *Optics*, 4th edition, Addison-Wesley, San Francisco (2002).

[7] E.W. Thulstrup and J. Michl, *Elementary Polarization Spectroscopy*, 2nd edition, Wiley, New York (1997).

[8] R. A. Chipman, "Polarimetry," Chap. 22 in *Handbook of Optics*, 2nd ed., M. Bass, Ed., Vol. 2, pp. 22.1–22.37, McGraw-Hill, New York (1994).

[9] W.S. Bickel and W.M. Bailey, "Stokes vectors, Mueller matrices, and polarization of scattered light," *Am. J. Phys*. **53**, 468–478 (1985).

[10] S. Yau Lu and R.A. Chipman, "Interpretation of Mueller matrices based on polar decomposition," *J. Opt. Soc. Am. A* **13**, 1106–1113 (1996).

[11] S.L. Jacques, J.C. Ramella-Roman, and K. Lee, "Imaging skin pathology with polarized light," *J. Biomed. Opt.* **7**, 329–340 (2002).

[12] N. Ghosh, M.F.G. Wood, and I.A. Vitkin, "Polarized light assessment of complex turbid media such as biological tissues using Mueller matrix decomposition"; Chapter 9, *Handbook of Photonics for Biomedical Science*, Ed. by Valery V. Tuchin, CRC Press, Taylor & Francis Group, London, pp.253–282 (2010).

[13] M.F.G. Wood, N. Ghosh, X. Guo, and I.A. Vitkin, "Towards noninvasive glucose sensing using polarization analysis of multiply scattered light"; Chapter 17, *Handbook of Optical Sensing of Glucose in Biological Fluids and Tissues*, Ed. by Valery V. Tuchin, Series in Medical Physics and Biomedical Engineering Volume: 12, CRC Press, Taylor & Francis Group, London (2008), pp. 527?558.

[14] R.J. McNichols and G.L. Côté, "Optical glucose sensing in biological fluids: an overview," *J. Biomed. Opt.* **5**, 5–16 (2000).

[15] E. Collett, "Measurement of the four Stokes polarization parameters with a single circular polarizer," *Opt. Commun*. **52**, 77–80 (1984).

[16] V. Sankaran, K. Schonenberger, J.T. Walsh Jr., and D.J. Maitland, "Polarization discrimination of coherently propagating light in turbid media," *Appl. Opt.* **38**, 4252–4261 (1999).

[17] V. Sankaran, J.T. Walsh, Jr., and D.J. Maitland, "Comparative study of polarized light propagation in biological tissues," *J. Biomed. Opt.* **7**, 300–306 (2002).

[18] N. Ghosh, A. Pradhan, P.K. Gupta, S. Gupta, V. Jaiswal, and R.P. Singh, "Depolarization of light in a multiply scattering medium: effect of refractive index of scatterer," *Phys. Rev. E,* **70**, 066607 (2004).

[19] N. Ghosh, P.K. Gupta, A. Pradhan, and S.K. Majumder, "Anomalous behavior of depolarization of light in a turbid medium," *Phys. Lett. A* **354**, 236–242 (2006).

[20] N. Ghosh, H.S. Patel, and P.K. Gupta, "Depolarization of light in tissue phantoms – effect of a distribution in the size of scatterers," *Opt. Exp.* **11**, 2198–2205 (2003).

[21] X. Guo, M. F. G. Wood, and I. A. Vitkin, "Angular measurement of light scattered by turbid chiral media using linear Stokes polarimetry," *J. Biomed. Opt.* **11**, 041105 (2006).

[22] M. Abramowitz and I. Stegun, *Handbook of Mathematical Functions with Formulas, Graphs, and Mathematical Tables*, National Institute of Standards and Technology, Washington, D.C., 1964.

[23] W. Guan, G.A. Jones, Y. Liu, and T.H. Shen, "The measurement of the Stokes parameters: a generalized methodology using a dual photoelastic modulator system," *J. Appl. Phys.* **103**, 043104 (2008).

[24] A. Ambirajan and D.C. Look, Jr., "Optimum angles for a polarimeter: part I," *Opt. Eng.,* **34**, 1651–1655 (1995).

[25] D.S. Sabatke, M.R. Descour , E.L. Dereniak, W.C. Sweatt, S.A. Kemme, and G.S. Phipps, "Optimization of retardance for a complete Stokes polarimeter," Opt. Lett. 25, 802–804 (2000).

[26] S.N. Savenkov, "Optimization and structuring of the instrument matrix for polarimetric measurements," *Opt. Eng.*, 41, 965–972 (2002).

[27] D. Layden, M.F.G. Wood, and I.A. Vitkin, "Optimum selection of input polarization states in determining the sample Mueller matrix: a dual photoelastic polarimeter approach," *Opt. Exp.* (2012, in press).

[28] E. Collett, *Field Guide to Polarization*, SPIE Press: Bellingham, WA (2005).

[29] N. Ghosh, M.F.G. Wood, and I.A. Vitkin, "Mueller matrix decomposition for extraction of individual polarization parameters from complex turbid media exhibiting multiple scattering, optical activity and linear birefringence," *J. Biomed. Opt.* **13**, 044036 (2008).

[30] N. Ghosh, M.F.G. Wood, S.-H. Li, R.D. Weisel, B.C. Wilson, Ren-Ke Li, and I.A. Vitkin, "Mueller matrix decomposition for polarized light assessment of biological tissues," *J. Biophotonics,* **2**, 145–156 (2009).

[31] R.M.A. Azzam, "Photopolarimetric measurement of the Mueller matrix by Fourier analysis of a single detected signal," *Opt. Lett.* **2**, 148–150 (1978).

[32] D.H. Goldstein, "Mueller matrix dual-rotating retarder polarimeter," *Appl. Opt.* **31**, 6676–6683 (1990).

[33] M.H. Smith, "Optimization of a dual-rotating-retarder Mueller matrix polarimeter," *Appl. Opt.* **41**, 2488–2493 (2002).

[34] M. Dubreuil, S. Rivet, B. Le Jeune, and J. Cariou, "Snapshot Mueller matrix polarimeter by wavelength polarization coding," *Opt. Express*, **15,** 13660 (2007).

[35] J.S. Baba, J.R. Chung, A.H. DeLaughter, B.D. Cameron, and G.L. Côté, "Development and calibration of an automated Mueller matrix polarization imaging system," *J. Biomed. Opt.* **7**, 341–348 (2002).

[36] A. De Martino, E. Garcia-Caurel, B. Laude, and B. Drévillon, "General methods for optimized design and calibration of Mueller polarimeters," *Thin Solid Films* **455** , 112–119 (2004).

[37] B. Laude-Boulesteix, A. de Martino, B. Drévillon, and L. Schwartz, "Mueller polarimetric imaging system with liquid crystals," *Appl. Opt.* **43**, 2824–2832 (2004).

[38] M. Mujat and A. Dogariu, "Real-time measurement of the polarization transfer function," *Appl. Opt.* **40**, 34–44 (2001).

[39] E. Compain, S. Poirier, and B. Drevillon, "General and self-consistent method for the calibration of polarization modulators, polarimeters, and Mueller-matrix ellipsometers," *Appl. Opt.* **38**, 3490–3502 (1999).

[40] C.-Y. Han and Y.-F. Chao, "Photoelastic modulated imaging ellipsometry by stroboscopic illumination technique," *Rev. Sci. Instrum.* **77**, 023107 (2006).

[41] R.M. Azzam and N.M. Bashara, *Ellipsometry and Polarized Light*, North Holland, Amsterdam (1979).

[42] V.V. Tuchin, L. Wang, and D.A. Zimnyakov, *Optical Polarization in Biomedical Applications*, Springer-Verlag, New York (2006).

[43] A.J. Welch, M.J.C Van Germert, W.M. Star and B.C. Wilson, "Overview of tissue optical properties," in *Optical thermal response of laser irradiated tissue*, A.J. Welch and M.J.C. Van Germert, Eds., Plenum, New York (1995).

[44] A. Ishimaru, *Wave Propagation and Scattering in Random Media*, Academic Press, New York (1978).

[45] D. Bicout, C. Brosseau , A.S. Martinez, and J.M. Schmitt , "Depolarization of multiply scattered waves by spherical diffusers: Influence of size parameter," *Phys. Rev. E* **49**, 1767–1770 (1994).

[46] E.E. Gorodnichev, A.I. Kuzolov, and D.B. Rozozkin, "Diffusion of circularly polarized light in a disordered medium with large scale inhomogeneities," *JETP Letters* **68**, 22–28 (1998).

[47] A.D. Kim and M. Moscoso, "Influence of the refractive index on the depolarization of multiply scattered wave," *Phys. Rev. E* **64**, 026612 (2001).

[48] M. Xu and R. R. Alfano, "Random walk of polarized light in turbid media," *Phys. Rev. Lett.* **95**, 213901 (2005).

[49] N. Ghosh and I.A. Vitkin, "Tissue polarimetry: concepts, challenges, applications and outlook," *J. Biomed. Opt.* **16**, 110801, (2011).

[50] L. Wang, S.L. Jacques, and L. Zheng, "MCML—Monte Carlo modeling of light transport in multi-layered tissues," *Comput. Methods Programs Biomed.* **47**, 131–146 (1995).

[51] M. Moscoso, J.B. Keller, and G. Papanicolaou, "Depolarization and blurring of optical images by biological tissue," *J. Opt. Soc. Am. A* **18**, 948–960 (2001).

[52] M.F.G. Wood, X. Guo, and I.A. Vitkin, "Polarized light propagation in multiply scattering media exhibiting both linear birefringence and optical activity: Monte Carlo model and experimental methodology," *J. Biomed. Opt.* **12**, 014029 (2007).

[53] M. Xu.,"Electric field Monte Carlo for polarized light propagation in turbid media," *Opt. Exp.* **12**, 6530–6539 (2004).

[54] J.C. Ramella-Roman, S.A. Prahl, and S.L. Jacques, ''Three Monte Carlo programs of polarized light transport into scattering media: part I," *Opt. Exp.* **13**, 4420–4438 (2005).

[55] D. Côté and I.A. Vitkin, "Robust concentration determination of optically active molecules in turbid media with validated three-dimensional polarization sensitive Monte Carlo calculations," *Opt. Express* **13**, 148-163 (2005).

[56] R. Clark Jones, "New calculus for the treatment of optical systems. VII. Properties of the N-matrices," *J. Opt. Soc. Am.* **38**, 671–685 (1948).

[57] L.V. Wang, G.L Côté, and S. L. Jacques, "Special section guest editorial: tissue polarimetry," *J. Biomed. Opt*. **7**, 278 (2002).

[58] S. Manhas, M.K. Swami, P. Buddhiwant, N. Ghosh, P.K. Gupta, and K. Singh, "Mueller matrix approach for determination of optical rotation in chiral turbid media in backscattering geometry," *Opt. Exp*. **14**, 190–202 (2006).

[59] P.J. Wu and J.T. Walsh Jr.,"Stokes polarimetry imaging of rat tail tissue in a turbid medium: degree of linear polarization image maps using incident linearly polarized ligh," *J. Biomed. Opt*. **11**, 014031 (2006).

[60] R. Ossikovski, A. De Martino, and S. Guyot, "Forward and reverse product decompositions of depolarizing Mueller matrices," *Opt. Lett*. **32**, 689–691 (2007).

[61] R. Ossikovski, "Analysis of depolarizing Mueller matrices through a symmetric decomposition," *J. Opt. Soc. Am. A* **26**, 1109–1118 (2009).

[62] R. Ossikovski, "Differential matrix formalism for depolarizing anisotropic media," *Opt. Lett.* **36**, 2330–2332 (2011).

[63] R.M.A. Azzam, "Propagation of partially polarized light through anisotropic media with or without depolarization: A differential 4×4 matrix calculus," *J. Opt. Soc. Am.* **68**, 1756–1767 (1978).

[64] R. Ossikovski et al., "Depolarizing Mueller matrices: how to decompose them?," *Phys. Stat. Sol.* (a) **205**, 720–727 (2008).

[65] N. Ghosh, M.F.G. Wood, and I.A. Vitkin, "Polarimetry in turbid, birefringent, optically active media: a Monte Carlo study of Mueller matrix decomposition in the backscattering geometry," *J. Appl. Phys*. **105**, 102023 (2009).

[66] M.F.G. Wood, N. Ghosh, E.H. Moriyama, B.C. Wilson, and I.A. Vitkin, "Proof-of-principle demonstration of a Mueller matrix decomposition method for polarized light tissue characterization *in vivo*," *J. Biomed. Opt.* **14**, 014029 (2009).

[67] N. Ghosh, M.F.G. Wood, and I.A. Vitkin, "Influence of the order of the constituent basis matrices on the Mueller matrix decomposition-derived polarization parameters in complex turbid media such as biological tissues," *Opt. Commun*. **283**, 1200–1208 (2010).

[68] S.L. Jacques, "Polarized light imaging of biological tissues," in *Handbook of Biomedical Optics*, chapter 30, edited by D. Boas, C. Pitris and N. Ramanujam, CRC Press, Boca Raton, Florida (2011)

[69] S. Brasselet , "Polarization-resolved nonlinear microscopy: application to structural molecular and biological imaging," *Advances in Optics and Photonics* **3** 205–271 (2011)

[70] C.A. Browne and F.W. Zerban, *Physical and Chemical Methods of Sugar Analysis*, Wiley, New York (1941).

[71] D. Côt´ and I.A. Vitkin, "Balanced detection for low-noise precision polarimetric measurements of optically active, multiply scattering tissue phantoms," *J. Biomed. Opt.* **9**, 213–220 (2004).

[72] M.F.G. Wood, D. Côté, and I.A. Vitkin, "Combined optical intensity and polarization methodology for analyte concentration determination in simulated optically clear and turbid biological media," *J. Biomed. Opt*. **13**, 044037 (2008).

[73] D. Goldstein, *Polarized Light*, 2nd edition, Marcel Dekker, New York (2003).

[74] D. Orlic, et al., "Bone marrow cells regenerate infarcted myocardium," *Nature* **410**, 701–705 (2001).

[75] M.F.G. Wood, N. Ghosh, M.A. Wallenburg, S.-H. Li, R.D. Weisel, B.C. Wilson, R.-K. Li, and I.A. Vitkin, "Polarization birefringence measurements for characterizing the myocardium, including healthy, infracted, and stem cell treated regenerating cardiac tissues," *J. Biomed. Opt.* **15**, 047009 (2010).

[76] S.-H. Li, Z. Sun, L. Guo, M. Han, M.F.G. Wood, N. Ghosh, I.A. Vitkin, R.D. Weisel, and R.-K. Li, "Elastin gene over-expression during cell therapy prevents scar expansion and ventricular dysfunction after myocardial infarction," *J. Molec. Cell Cardiol.* 2012 (in press)

[77] J. Chung et al., "Use of polar decomposition for the diagnosis of oral precancer," *Appl. Opt*. **46**, 3038–3044 (2007).

[78] P. Shukla and A. Pradhan, "Mueller decomposition images for cervical tissue: Potential for discriminating normal and dysplastic states," *Opt. Exp*. **17**, 1600–1609 (2009).

[79] S. Manhas, M.K. Swami, H.S. Patel, A. Uppal, N. Ghosh, and P.K. Gupta, "Polarized diffuse reflectance measurements on cancerous and noncancerous tissues," *J. Biophotonics* **2**, 581–587 (2009).

[80] M.A. Wallenburg, M.F.G. Wood, N. Ghosh, and I.A. Vitkin, "Polarimetry-based method to extract geometry-independent metrics of tissue anisotropy," *Opt. Lett.,* **35**, 2570–2572 (2010).

[81] M.A. Wallenburg, M. Pop, M.F.G. Wood, N. Ghosh, G.A. Wright, and I.A. Vitkin, "Comparison of optical polarimetry and diffusion tensor MR imaging for assessing myocardial anisotropy," *J. Innov. Opt. Health Sci.* **3,** 109–121 (2010).

[82] M.A. Wallenburg, S.-H. Li, R.-K. Li, and I. A. Vitkin, "Two photon microscopy of healthy, infarcted, and regenerating myocardium," *J. Biophoton.* **4** 297–304, (2011)

[83] K.J. Aitken and D.J. Bagli, "The bladder extracellular matrix. Part I: architecture, development and disease," *Nat. Rev. Urol.* **6**, 596–611 (2009).

[84] K.J. Aitken and D.J. Bagli, "The bladder extracellular matrix. Part II: regenerative applications," *Nat. Rev. Urol.* **6**, 612–21 (2009).

[85] T. Berrocal, P. Lopez-Pereira, A. Arjonilla, and J. Gutierrez, "Anomalies of the distal ureter, bladder, and urethra in children: embryologic, radiologic, and pathologic features," *Radiographics* **22**, 1139–1164 (2002).

[86] A. Tubaro, C. De Nunzio, A. Trucchi, G. Palleschi, and L. Miano, "The effect of bladder outlet obstruction treatment on ultrasound-determined bladder wall thickness," *Rev. Urol.* **7**, S35-42 (2005).

[87] C.C. Wang, J. Nagatomi, K.K. Toosi, N. Yoshimura, J.H. Hsieh, M.B. Chancellor, and M. Sacks, "Diabetes-induced alternations in biomechanical properties of urinary bladder wall in rats" *Urology* **73**, 911-5 (2009).

[88] S. Alali, K. Aitken, D. Bagli, and I.A. Vitkin, "Optical assessment of anisotropy in ex-vivo distended rat bladders," *J. Biomed. Opt.* (2012, in press)

[89] G.S. Jack, R. Zhang, M. Lee, Y. Xu, B.M. Wu, and L.V. Rodrigues, "Urinary bladder smooth muscle engineered from adipose stem cells and a three dimensional synthetic composite," *Biomaterials* **30**, 3259-70 (2009).

[90] R.L. Heise, J. Ivanova, A. Parek, and M.A. Sacks, "Generating elastin-rich small intestinal submucosa-based smooth muscle constructs utilizing exogenous growth factors and cyclic mechanical stimulation," *Tissue Eng. Part A* **15,** 3951-60 (2009).